

Development of pH-Sensitive Nanoparticles for the Combined Chemo- Immunotherapy of Cancer

by

KAVYA SREE MARVAJJALA

Under the Supervision of

Dr. ANIRUDDHA ROY



**BIRLA INSTITUTE OF TECHNOLOGY AND SCIENCE,
PILANI CAMPUS, RAJASTHAN**

Introduction

Even after decades of research for the development of advanced therapeutics, breast cancer remained the leading cause of cancer-associated death among women worldwide.¹ While mortality from other cancers has shown a gradual decline over the years, breast cancer mortality significantly increased from 1990 to 2017.² Development of different subtypes, including triple-negative breast cancer (TNBC), makes therapeutic prognosis even poorer.³ It has been observed that almost all types of breast cancers exhibit a significant increase in the infiltration of macrophages in the tumor.⁴ These macrophages facilitate malignancy and promote therapy evasion and metastatic progression.

Cancer has been considered a disease of the neoplastic cells for a long time. Due to this, cancer cells are the lone target against which almost all the anti-cancer drugs were developed, and chemotherapy has become the first-line therapy in most cancers, including breast cancer. However, the prognosis remained poor due to high toxicity and the development of drug resistance.⁵ Many advanced studies have now established that cancer is supported by a complex interaction of neoplastic and non-neoplastic cells in a strong symbiotic relationship that helps the growth and progression of the malignant cells.⁶ Conversely, most of the current therapeutic strategies against cancer are one-dimensional, i.e., it is directed against only one component (cancer cells) of the complex, multi-integrant tumor ecosystem. With most of these single-pronged therapeutic strategies, tumor regression was initially seen due to the death of bulk neoplastic cells; however, these tumors can relapse with aggressive resistant phenotypes developed due to modulation by the dynamic tumor microenvironment(TME).⁷⁻⁹ For a more successful treatment, multi-dimensional treatment modalities targeting different components of the tumor ecosystem need to be developed.

Among different non-neoplastic cells present in the TME, tumor-associated immune cells play one of the most critical tumor-promoting roles by increasing angiogenesis, modifying other stromal cells, and maintaining an immune inhibitory milieu.¹⁰ However, if adequately activated, these immune cells can become tumoricidal, as shown by multiple studies.¹¹ Activating the immune cells in the TME against the cancer cells is a multistep process. Antigen-presenting cells (APC) like macrophages and dendritic cells play one of the most critical roles in this process, as, without effective antigen presentation and co-stimulatory signals, no T-cell activation would occur. The primary APCs present in the tumor is tumor-associated macrophages (TAMs).¹² However, TAMs maintain an immunosuppressive TME by producing

a host of immune inhibitory cytokines, including CCL2, TGF- β , and IL-10, and convert effector T-cells to regulatory T-cells.¹³ Re-educating these TAMs from their immunosuppressive state to the immune-stimulatory phenotype can be a potential strategy for a successful anti-tumor response.¹⁴ Toll-like receptor (TLR) agonists are one of the most potent ligands for activating macrophages. It has been proven that TLR7/8 agonists have enhanced immune response in mouse models of breast cancer.¹⁵ poly-IC, a synthetic double-stranded RNA targeting TLR3, has shown promising efficacy in a Phase II clinical trial against breast cancer.¹⁶ In the current study, initial screening of different TLR agonists was performed to evaluate their immune stimulatory activity. Among all the TLR-agonists screened, resiquimod (RSQ) was the most effective. RSQ is a TLR7 and 8 agonist, which has shown significant TAM activation capability in multiple studies.¹⁷⁻¹⁹ However, though highly effective for cancer immunotherapy, no systemic formulation of RSQ is available due to its solubility and toxicity problem, limiting its use. Also, as cancer cells are responsible for nurturing the immunosuppressive TME, activating the anti-tumor immune response is highly challenging without tumor depletion. Chemotherapeutic drugs can be used for this purpose. Unfortunately, most chemotherapeutic drugs are immunosuppressive, hence not helpful. One significant exception is paclitaxel (PTX), a potent anti-cancer agent that has been approved for the treatment of breast, ovarian and other cancers.²⁰ PTX has shown immune stimulatory activity, including increased accumulation and activation of effector T cells, dendritic cells (DCs), natural killer (NK) cells, and macrophages.²¹ Henceforth, co-delivery of PTX and RSQ can be highly effective for combined chemo-immunotherapy of breast cancer. Delivery of a multi-dimensional drug combination is more complicated than delivering a single drug. As different drugs target different cells, their bioavailability in the TME is critical. For delivery of a combination of drugs, an ideal delivery system should protect the drugs from metabolism during systemic circulation, minimize non-specific accumulation in normal tissues, and upon reaching the TME, should release the drugs to act on their specific targets. For this purpose, triggering the release of the drugs from the NPs at the TME can be an effective strategy, by exploiting the acidic extracellular pH of the TME.²² This study aimed to evaluate the *in-vitro* efficacy of PTX and RSQ combination against breast cancer and to develop a unique pH-responsive NP to deliver this drug combination. The objective was to synthesize a pH-responsive polymer, formulate an NP system using that polymer co-encapsulating PTX and RSQ, evaluate the pH-responsive behavior of the NPs, as well as to analyze the *in-vitro* bioefficacy of the drug-loaded NPs in a cancer cell–macrophage co-culture system using 2D as well as 3D multi-cellular breast cancer spheroid model and *in-vivo* in terms of

pharmacokinetic profile followed by tumor biodistribution and in-vivo anticancer efficacy along with metastasis profiling in orthotopic breast cancer model.

Objectives of proposed work

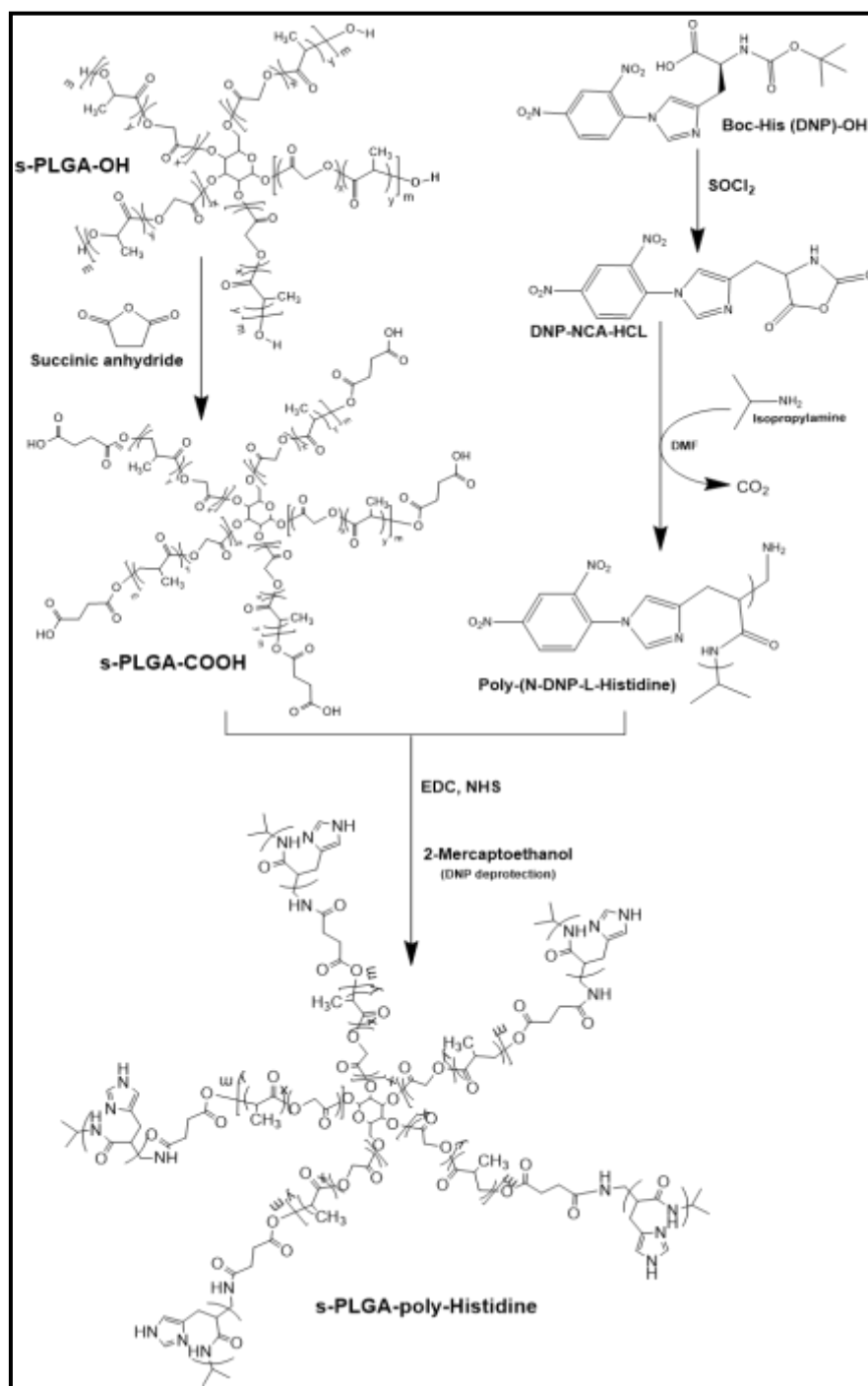
1. Screening of anticancer drugs and immunomodulators for synergistic anticancer efficacy. Preparation of a pH-sensitive nanoparticle encapsulating the selected chemotherapeutic agent and immunomodulator.
2. Physicochemical characterization of the nanoparticles in terms of size, polydispersity, encapsulation efficiency, stability, and drug release profile.
3. Determination of the pharmacological activity of the combination therapy in the in-vitro model using both 2D and 3D co-culture systems. Analysis of the synergy and the molecular mechanism responsible.
4. In-vivo pharmacokinetic and bio-distribution analysis. Efficacy study in orthotopic mouse tumor model.

Materials and Methods

Chemicals and reagents:

PTX was received as a gift sample from INTAS Pharmaceuticals Ltd, and RSQ was purchased from TCI, India. Acetonitrile (HPLC grade), diethyl ether (DEE), chloroform (CHCl₃), dimethylformamide (DMF), dimethyl sulfoxide (DMSO), and methanol were procured from Merck, India. Hydroxyl-terminated linear PLGA, hydroxyl-terminated star-shaped PLGA, Boc-His(Dnp)-OH, N-(3-Dimethylaminopropyl)-N'-ethyl carbodiimide hydrochloride (EDC), 4-(dimethylamine)pyridine (DMAP), 3-(4,5-dimethylthiazol-2-yl)-2,5-diphenyltetrazolium bromide (MTT) were purchased from Sigma-Aldrich. cDNA synthesis kit and SYBR green qPCR kit were purchased from Bio-Rad. 2-mercaptoethanol was purchased from SRL, India. HPLC analysis was done using a Shimadzu LC instrument (Kyoto, Japan). Zodiac C-18 column (5 µm particle size, L × I.D. 15 cm × 4.6 mm) was used as the stationary phase. Micromixer chip and MitoS Duo XS-Pump, used for formulation, were purchased from Dolomite, Royston, UK. All other chemical reagents used were of A.R. grade.

Synthesis of pH-sensitive polymers: Linear PLGA-poly-histidine (l-PLGA-pH) and star PLGA-poly-histidine (s-PLGA-pH)



Scheme 1: Reaction scheme for the synthesis of s-PLGA-pH

s-PLGA-OH (100mg) was reacted with succinic anhydride (20mg) in the presence of DMAP (20mg) in 1mL of anhydrous acetonitrile and was kept for continuous stirring for 24h in N_2 atmosphere at room temperature, which resulted in the formation of s-PLGA-COOH. It was then purified using 50 ml of ice-cold DEE and repeated 3 times to remove the unreacted

polymer. Boc-His(DNP)-OH (1g) was suspended in 10mL of anhydrous acetonitrile, and 1mL of thionyl chloride was added dropwise under continuous stirring in an N₂ atmosphere for 1h for the formation of DNP-NCA-HCl. The product was precipitated using 100ml of ice-cold DEE with consecutive washing for 3 times (50ml each). Then, the obtained product DNP-NCA-HCl was dissolved in 10mL of anhydrous DMF, and then for ring-opening polymerization, isopropylamine (1mL) was added, the product poly-(N-DNP-L-histidine) was purified by precipitation in an excess of ice-cold DEE in order to remove the unreacted reactants. Then, poly-(N-DNP-L-histidine) was reacted with s-PLGA-COOH in EDC and NHS to form-PLGA-poly-histidine-(DNP). DNP deprotection was carried out by reacting s-PLGA-poly-histidine-(DNP) with 1mL of 50% 2-mercaptoethanol in DMF for 12h with continuous stirring and then precipitated by using 100ml of ice-cold DEE for 72 h, repeated for 3 times to obtain the final product s-PLGA-poly-histidine (s-PLGA-pH). The obtained residue was washed with Milli-Q, then lyophilized for 24h and stored at -20°C.

l-PLGA-pH was synthesized by conjugating l-PLGA-COOH with poly-histidine in EDC and NHS to obtain l-PLGA-poly-histidine-(DNP) followed by DNP deprotection and purification as that of s-PLGA-pH.

Structural identification of the synthesized pH-sensitive polymer

¹H NMR and FTIR analyses were performed to confirm the formation of s-PLGA-pH and l-PLGA-pH. The chemical structures of s-PLGA, Boc-His (DNP)-OH, DNP-NCA-HCL, poly-histidine, s-PLGA-pH, and l-PLGA-pH were characterized by ¹H NMR spectroscopy at 300 MHz on a Bruker Avance spectrometer using tetramethyl silane as an internal standard. FTIR spectra in the range of 4000 to 400 cm⁻¹ were also acquired using ATR-IR using a Bruker ATR-IR machine.

Preparation of drug-loaded NPs

The nanoprecipitation-based method used microfluidic technology to prepare s-PLGA-pH and l-PLGA-pH NPs loaded with PTX and RSQ. Briefly, 0.5% Soluplus solution was used as the aqueous phase. PTX (100ug), RSQ (2mg), and s-PLGA-pH (20mg) were dissolved in 1 mL ACN, which was used as the organic phase. Two separate pumps dispensed both the aqueous and organic phases at a 100 µL/min flow rate for the aqueous phase and 10µL/min for the organic phase. Outlets of organic and aqueous pumps (A&B) were introduced into the micromixer chip, combining the two solutions using a 'T' junction. Here, both the aqueous and

organic phases were mixed by hydrodynamic flow focusing and staggered herringbone mixing, leading to the formation of the NPs due to nanoprecipitation of the polymer and drugs after mixing with the aqueous phase. These NPs were then collected and stirred overnight for the evaporation of ACN. Residual solvent and untrapped (free) drugs were removed by dialyzing with an MWCO membrane of 10,000 Da (HiMedia) for 24h using 500ml of MQ water as an external medium with two water changes at 6h and 12h. NPs were then concentrated by centrifugation at 2000 g for 15 minutes. To obtain a 1:200 molar ratio of PTX: RSQ loading in NPs, variable drug concentrations were observed for entrapment and drug loading in the initial screening. DiI-loaded NPs were prepared similarly, where 1mg of DiI and 20mg of polymer were dissolved in 1 ml of ACN and used as the organic phase and 10 ml of 0.5% Soluplus solution was used as the aqueous phase. As discussed earlier, NPs were prepared using microfluidics, followed by solvent evaporation and free drug removal by dialysis.

HPLC method for simultaneous estimation of PTX and RSQ

An HPLC method was developed to estimate both the drugs (PTX and RSQ) simultaneously. Briefly, HPLC analysis was done using a Zodiac C18 column as the stationary phase and ACN: pH 5 phosphate buffer (60:40) as the mobile phase, with a flow rate of 1mL/min and 10min run time. The column oven temperature was 40°C. HPLC analyses of all the samples were performed using a 20µL injection volume, where the samples were dissolved in 60% ACN. The linearity curve was plotted for both PTX and RSQ, $R^2=0.99$. The limit of detection (LOD) was found to be 0.04µg/mL, 0.075 µg/mL for PTX and RSQ, respectively, and the limit of quantification (LOQ) was found to be 0.14µg/mL and 0.2 µg/mL for PTX and RSQ respectively. Both LOD and LOQ were calculated according to ICH guidelines.

Drug loading and encapsulation in NPs

5 mg of NP was taken and dissolved in 200µL of ACN, vortexed for 15 min and s-PLGA/s-PLGA-pH/l-PLGA/ l-PLGA-pH NPs were precipitated by adding 1mL of methanol. The polymers were separated by centrifuging at 3000g for 30 min. The supernatant was collected, dried, and dissolved in 60% ACN before being analyzed with HPLC.

The entrapment efficiency of the NPs was calculated by using the formula:

$$\% \text{ Entrapment efficiency (\%EE)} = \left(\frac{\text{Weight of actual drug loaded}}{\text{Total weight of drug added initially.}} \right) \times 100$$

Loading capacity was calculated by using the formula:

$$\% \text{ Loading capacity (\%LC)} = \left(\frac{\text{Weight of total drug loading}}{\text{Total NP weight}} \right) \times 100$$

Analysis of particle size, polydispersity index (PDI), and zeta potential

The mean particle size, polydispersity index (PDI), and zeta potential of the NPs were measured using Zetasizer Nano ZS, Malvern Instruments, UK, at a backscattering angle of 173°.

Analysis of the pH-dependent size variation of the nanoparticles

s-PLGA, l-PLGA, s-PLGA-pH, and l-PLGA-pH NPs 5mg/ml were dispersed in pH 7.4 and 6.5 phosphate buffers. Particle sizes and PDI of NPs were analyzed using DLS at 6h time point. In addition to DLS, the pH-dependent change in the NP morphology was analyzed by field emission scanning electron microscopy (FESEM) after suspending the NPs for 3h in a pH 7.4 and 6.5 buffer. After that, the NP suspension was air-dried, placed on the sample stub using double-sided carbon tape, and gold coated. These were then subjected to FESEM analysis.

***In-vitro* drug release study**

The drug release studies in different pH buffers were performed using dialysis. In brief, 5mg of the drugs-loaded NPs (s-PLGA (0.59µgPTX +53µg RSQ), l-PLGA (0.6µg PTX +58µg RSQ), s-PLGA-pH(0.64µg PTX +58µg RSQ), and l-PLGA-pH(0.7µgPTX +56µg RSQ) NPs) was diluted in 1mL of release medium in a dialysis bag and kept in a beaker containing 20mL of release medium (20 mM phosphate-buffered solution, pH 6.5 and 7.4). Sink condition was maintained using 0.2% tween 80 in the medium and kept on a magnetic stirrer (150 rpm) at 37°C. At 0, 0.25, 0.5, 1, 3, 6, 12, 24, 48, and 72h time intervals, 500 µL of the sample was collected and replaced with the same amount of buffer. The collected samples were then mixed with an equal volume of ACN and centrifuged at 3000×g for 30 min. The supernatant was taken and further analyzed using HPLC. Cumulative drug release (CDR) was calculated as follows:

$$\% \text{ Cumulative release (\% CDR)} = \left(\frac{\text{Drug released from the NPs at the time 't'}}{\text{Amount of drug present in NPs}} \right) \times 100$$

Cell culture

4T1 (a breast cancer cell line derived from the mammary gland tissue of a mouse BALB/c strain) and RAW 264.7 (mouse monocyte-macrophage cell line) were separately cultured in Dulbecco's Modified Eagle Medium (DMEM), supplemented with 10% fetal bovine serum and 50 units/mL penicillin, and 50 mg/mL streptomycin at 37 °C, 5%CO₂ in a humidified atmosphere. Cells were sub-cultured at 90% confluency using Trypsin–EDTA solution (0.05%) for cell detachment.

Cancer-macrophage co-culture and complex spheroid model

For the NP penetration study and cytotoxicity study, 4T1+RAW 264.7 spheroids were prepared. Briefly, cells (7,500 4T1 cells and 2,500 RAW 264.7) at 10,000 cells / 10µl (in 0.2% methyl cellulose-containing cell culture medium) were placed as hanging drops on the lid of the cell culture Petri dish. The hanging drops were kept humidified by putting PBS in the base of the Petri dish to prevent drying of the spheroid. After that, the hanging drops were transferred to 1% agarose-coated round bottom 96 well plates with 200 µl cell culture medium and incubated for 24 h, yielding the 4T1+RAW 264.7 spheroids.

For RNA isolation from RAW 246.7 cells after co-culture with 4T1, only 4T1 spheroids were made and co-cultured with RAW 246.7. Briefly, 4T1 cells at 10,000 cells / 10µl (0.2% methyl cellulose-containing cell culture medium) were placed as hanging drops on the lid of the cell culture Petri dish. Spheroids were humidified by putting PBS in a Petri dish. After 24 h of incubation, spheroids were transferred into 1% agarose coated wells (in 24 well plate) with 1 mL cell culture medium. Then RAW 246.7 cells at a density of 10,000 cells were plated on a transwell (0.4 µm, polycarbonate membrane) inserted in 4T1 spheroids (5 spheroids per well) containing well.

Cytotoxicity assay (2D and 3D)

For cell viability assay of 2D culture, 4T1/RAW cells were seeded at the density of 5000 cells/well in a 96-well plate. After 24 h of incubation, cells were treated with drug solutions (0.5-500 nM PTX, 0.1-1µM RSQ in the initial screening, and 5nM PTX and 1µM RSQ in further studies) and incubated for 72 h at 37 °C with 5% CO₂. No drug treatment was given in the control cells, and the same amount of complete medium was added. After 72h of incubation, cells were treated with 200µl of 1 mg/mL MTT solution dissolved in complete medium. After 4 h of incubation with MTT, the medium was replaced with 200 µl of DMSO to dissolve the

formazan crystal formed by the viable cells. Optical density at 570 nm was measured by removing background absorbance at 630 nm. Cell viability was calculated using the following formula:

$$\text{Cell Viability (\%)} = \left(\frac{\text{mean absorbance value of drug treated cells}}{\text{mean absorbance value of control}} \right) \times 100$$

For cell viability assay of 3D culture, treatment was given for 72 h with free drug and encapsulated drugs equivalent to 10nM PTX and 2μM RSQ. Further, the spheroids were collected into 1.5 mL centrifuge tubes with medium and centrifuged for 10 min at 200×g. The supernatant was removed and replaced with MTT (1mg/mL) containing medium. After 4 h of incubation, MTT was replaced with DMSO (500 μl) to dissolve the formazan crystals formed by the viable cells. Then cell viability was calculated, as mentioned earlier.

Tumor-specific cell death using Live-Dead Staining.

For identifying the tumor-specific cell death, we have used Transwell (Quasi 3D system); here, we have made 4T1 spheroids and added them in the lower chamber of the Transwell and Raw macrophages (2D) on the transwell membrane in the top chamber. After 72h of treatment, we stained both the 4T1 spheroids and 2D macrophages using Annexin (1 μg/mL) and Propidium Iodide (PI- 10 μg/mL) diluted with PBS. Annexin labels all the nuclei in blue of all the viable cells, and PI labels the nuclei of dead cells in red. The staining was attained after incubating it for 15 minutes in the dark at 37°C and then followed by microscopy analysis.

Spheroid penetration of NPs

4T1 and RAW 264.7 co-culture spheroids were prepared as described earlier. 3 days old spheroids were treated with DiI loaded NPs containing 10 μM of DiI loaded NPs containing 10 μM of DiI (DiI entrapment in l-PLGA, s-PLGA, l-PLGA-pH, and s-PLGA-pH was 88%, 87%, 85%, and 82% respectively. The volume of NP to get 10μM of DiI from 20mg/ml of DiI-loaded NPs was calculated using entrapment efficiency) after 24h incubation with NPs. Images of spheroids were captured by using ZEISS Axio Scope A1 microscope at 10X magnification, and the images were processed with Zen 2.3 software. The distribution of fluorescence intensity was calculated using ImageJ software.

Macrophage marker expression analysis

Total RNA was isolated using TRI reagent and was used to synthesize cDNA using a cDNA synthesis kit. Gene-specific primers were used for the amplification of templates. The qRT-PCR reactions were performed using the SYBR Green super mix, and the data was normalized against GAPDH as a housekeeping gene. The primers used for qRT-PCR are GAPDH F(5'-3') ACCCAGAAGACTGTGGATGG, R (3'-5') TCTAGACGGCAGGTCAGGTC, TNF- α F(5'-3') GCCTCTTCTCATTCTGCTTG, R (3'-5') CTGATGAGAGGGAGGCCATT, CD86 F(5'-3') ACGATGGACCCCAGATGCACCA, R (3'-5') GCGTCTCCACGGAAACAGCA, TGF- β F(5'-3') CCTGTCCAACTAAGGC, R (3'-5') GGTTTCTCATAGATGGCG, IL-10 F(5'-3') CCCTGGGTGAGAAGCTGAAG, R (3'-5') CACTGCCTTGCTCTTATTTTCACA. qRT-PCR studies were performed on CFX Thermal Cycler (Bio-Rad). The relative RNA expression was analyzed using the $2^{-(\Delta\Delta C(T))}$ method.

Animal procurement

Female Balb/C mice aged 5-7 weeks, with a weight range of 18-20 g, were procured from the National Centre for Laboratory Animal Sciences, National Institute of Nutrition in Hyderabad, India, with protocol no. IAEC/RES/31/08. The experiments were conducted per the Committee for Control and Supervision of Experiments on Animals (CPCSEA) guidelines. The mice were housed in standard cages with five individuals per cage within a temperature-controlled environment (23-24 °C) with a relative humidity of 50-60 %. They followed a 12-hour light/dark cycle and were provided with appropriate quantities of food and water.

Toxicity study

Female BALB/c mice weighing 20 ± 5 g were divided into six groups (Control, PTX, RSQ, PTX+RSQ, LpH, and spH) containing three mice. After overnight fasting, animals were treated with PTX (5 mg/kg), which was administered intravenously (i.v.) via tail vein, where 0.5 mg PTX in 100 μ l of ethanol+ 100 μ l of Tween 80 (1:1) and add 800 μ l of normal saline (N.S.). RSQ, Dissolve 19 mg RSQ in 100 μ l of ethanol+ 100 μ l of Tween 80 (1:1) and add 800 μ l of normal saline (N.S.). From this, inject 200 μ l through the tail vein (I.V.) into 20 g mice; for PTX+RSQ and NPs, equivalent doses were given through i.v. Route. The treatment was carried out with repeated doses at intervals of 0, 4, and 8. Animals were monitored regularly for skin color, eye color, fur levels, locomotion activity, water intake, tears production, abnormal stereotypy, and death recorded. After eight-day treatments, animals were sacrificed on the 8th

day, and all the major organs (Lungs, Liver, Kidneys, Heart, and Spleen) were collected, followed by slicing and H&E staining. The tissue sections were then captured using bright field microscopic imaging at 40× magnification.

H&E staining

Tissues were isolated, washed with saline, and fixed with 4% paraformaldehyde. Then, tissues were sliced at five µm thickness using a microtome. After mounting the slices on a glass slide, the manufacturer's protocol was followed with H & E staining. Histological modifications of tissue sections were performed using the light microscope.

Pharmacokinetic studies

Pharmacokinetic studies were performed on female BALB/c mice, 4-6 weeks old 20 ± 5 g; animals were divided into six groups (Control, PTX, RSQ, PTX+RSQ, LpH NPs, and spH NPs) with three animals in each group. Treatment for all the groups was administered by i.v. Route with the following doses: PTX (5mg/kg) and RSQ (150mg/kg). Equivalent amounts of PTX, RSQ in PR, LpH, and spH NPs were also administered through i.v. Route. By retro-orbital plexus, blood was collected at pre-determined time points from each animal (0.25, 1,2,4,6,12,24, 48, and 72h). Blood was collected into a tube containing 10% disodium EDTA as an anti-coagulant; plasma was isolated by centrifuging these tubes at 6,000 rpm for 15 minutes at 4 °C and then analyzed using HPLC. Plasma concentration Vs. Area profiles of PTX and RSQ were plotted. Different pharmacokinetic parameters, including area under the curve (AUC), apparent volume of distribution (Vd), drug concentration at $t = 0$ (C0), elimination half-life ($t_{1/2}$), and systemic plasma clearance were obtained by applying a non-compartmental model in Phoenix 8.0 WinNonlin (Pharsight Corporation, USA).

Establishment of the 4T1-Luc orthotopic tumor-bearing mice model

To study the tumor biodistribution and in-vivo efficacy of prepared NPs, we selected the 4T1-Luc orthotopic tumor-bearing mice model because this model has a high metastatic property. To establish the 4T1-Luc orthotopic breast cancer model, 100 µL of 4T1-Luc cell suspension (50,000 cells in 100 µL) was injected into the lower-left mammary fat pad of the female BALB/c mice.

Biodistribution study

The in-vivo biodistribution analysis of DiI-labeled nanoparticles (sp NPs and spH NPs) was conducted using an in-vivo imaging system (IVIS® Lumina III, PerkinElmer, USA). A dose of 100 µg/kg DiI equivalent of [DiI] sp NPs and [DiI] spH NPs was intravenously administered to BALB/c mice bearing 4T1-Luc tumors via the tail vein. Following injection, the biodistribution patterns were assessed at different time points (0.5, 1, 3, 6, 12, and 24 hours). Images were captured using the in-vivo imaging system with an excitation filter set at 550 nm and an emission filter set at 567 nm. Furthermore, 24 hours post-injection, the treated mice were euthanized. The main organs were collected, and ex-vivo images were acquired using the same in-vivo imaging system.

Tumor growth inhibition studies

4T1-Luc (1.5×10^6) cells were suspended in 100 µL of cold PBS and injected into the mammary fat pad of female Balb/c mice to induce tumor growth. Once the tumor volume reached 50-60 mm³, the mice were divided randomly into five groups (n = 5 each): control, PTX, RSQ, PTX+RSQ and spH NPs. Formulations were administered intravenously through the tail vein every other day for a period of 0, 4 days, and 8 days. The mice were regularly weighed during this period, and the tumor volume was recorded. On days 0, 5, 10, 15, and 21, the mice received intraperitoneal injections of D-luciferin (150 mg/kg), and imaging was conducted using IVIS Lumina (PerkinElmer Inc, USA; Ex/Em. 620/780 nm) to monitor tumor progression. After the completion of the treatment regimen, the mice were anesthetized using ketamine/xylazine; the tumors were surgically excised and weighed.

In-vivo lung metastasis analysis

After the surgical excision of tumors, the animals were allowed to recover. On the 9th day following the surgery, metastasis of the 4T1-Luc tumors was assessed through bioluminescence imaging using luciferin-D. Subsequently, the animals were euthanized, and their lungs were extracted. Changes in total lung weight resulting from tumor metastasis were determined by weighing the lungs. The lungs were then photographed, and the count of tumor nodules was recorded.

BrdU (Bromodeoxyuridine / 5-bromo-2'-deoxyuridine) is an analog of the thymidine nucleoside, commonly employed in the BrdU assay for identifying proliferating cells within cancer. To prepare a sterile solution of 10 mg/mL, BrdU was diluted in PBS. This solution, measuring 150 μ L, was intraperitoneally injected into distinct tumor-bearing mice on the 30th day post-tumor inoculation after each treatment. After a 2-hour interval, the lungs were surgically resected and then embedded in OCT media. The following day, the frozen lung exhibiting metastasis was sectioned via cryo-sectioning, producing slices with a thickness of 5 μ m. These sections underwent DNA denaturation using 1 N HCl for 10 minutes, followed by an additional 10-minute exposure to 2 N HCl, all performed at room temperature. Subsequently, the sections were immersed in 0.1 M borate buffer for 15 minutes, facilitating the removal of HCl, and then subjected to three 5-minute washes using 1% Triton X-100 in PBS with a pH of 7.4. To enhance permeability, the sections were exposed to 1.5% Triton X-100 in PBS for 1 hour, followed by an overnight incubation at 4°C with anti-BrdU rabbit IgG. On a subsequent day, the sections were subjected to a PBST wash, followed by a 1-hour incubation with a secondary anti-Rabbit IgG antibody. After a final PBS wash, the sections were examined under a fluorescence microscope.

To perform collagen I staining in metastatic lung tissue, 1% BSA-blocked tumor sections were incubated with Anti-Collagen I primary antibody (Abcam #ab138492) at a dilution of 1/1000, left overnight at 4°C. On the following day, the tissue sections underwent PBS washing and were subsequently incubated with Alexa Fluor® 488 secondary antibody for 2 hours in the dark at room temperature. After the 2 hours, the tissues were PBS-washed, treated with DAPI for 5 minutes, and then observed under a fluorescence microscope.

For hematoxylin and eosin (H&E) staining, lung tissue sections measuring 4 μ m in thickness were utilized. The sections were sequentially exposed to xylene, varying alcohol concentrations (30 % to 100 %), and water. Hematoxylin was employed to stain the nuclei, followed by thorough washing with tap water. Subsequently, eosin staining was applied to highlight the cytoplasm, followed by washing with dehydrated alcohol and xylene. The slides were then affixed using mounting media and inspected under a microscope with 10 \times magnification.

ROS detection assay

Reactive oxygen species (ROS) production within the tumor tissue was evaluated using the fluorescent probe DCFH-DA. Following a 21-day treatment regimen involving different drugs and formulations, an intratumoral injection of DCFH-DA (50 μ L, 25 μ M) was administered to

BALB/c mice bearing 4T1-Luc tumors. After a 30-minute incubation period, the mice were anesthetized and observed using an in-vivo imaging system (IVIS® Lumina III, PerkinElmer, USA). Subsequently, the tumors were isolated and cut into 5 µm-thick sections using a cryostat (Leica Biosystems, Germany). These tissue sections were subjected to staining with DAPI, mounted onto glass slides, and examined using a fluorescence microscope (Leica, Germany).

TUNEL assay

The assessment of apoptosis within the tumor tissues was conducted through the TUNEL assay. Tumor sections underwent treatment with the TUNEL reagent (TACS®TdT-Fluor). In Situ Apoptosis Detection Kit, R&D Systems, USA) following the guidelines provided by the manufacturer. Subsequently, the sections were examined using a fluorescence microscope. DAPI staining was observed using a blue filter (Ex/Em. 359/457 nm), while TUNEL-positive cells were visualized using a green filter (Ex/Em 488/520 nm).

Ki67 assay

Initially, tumor sections were incubated with a blocking buffer (1% BSA) for 1 hour. Following this, the sections were exposed to the Ki-67 primary antibody (Rabbit mAb #9129) for 12 hours at a temperature of 4°C. After being washed three times with PBS, the sections underwent an additional 2-hour incubation with a secondary antibody (Alexa Fluor® Plus 488) at room temperature in a dark environment. Following three additional washes with PBS, the sections were observed utilizing a fluorescent microscope.

Statistical analysis

The graphs and data were analyzed using Graph Pad Prism software version 7.0. The level of significance in all the panels was indicated by ** represents $p < 0.01$, *** represents $p < 0.001$, and **** represents $p < 0.0001$. One-way ANOVA was used when ≥ 2 groups were compared to the same control, and post hoc Tukey's test was performed to compare the means of each group with every other group. Two-way ANOVA was used for the studies, where two or more groups were compared with the control group with more than two variables. Post-hoc Bonferroni multiple comparison tests were used to compare the means of each group. Data were represented as mean \pm SD.

Results

Screening of TLR-agonists for macrophage stimulating efficacy

Initial screening was carried out using imiquimod (IMQ), Resiquimod (RSQ), and pidotimod (PTM) to find out their macrophage polarization efficacy against RAW 264.7 cell line (5,000 cells/ well). They all exhibited more than 100% macrophage viability, indicating no cellular toxicity at the dose range tested (0.1 μ M to 10 μ M) (**Figure 1A**). Next, macrophage stimulatory potency was evaluated by analyzing TNF- α expression, a primary anti-cancer macrophage activation marker. After treating RAW 264.7 cells (50,000 cells/well in a 6 well plate) with the drugs for 12 h, TNF- α expression was studied using qRT-PCR. Among all the TLR-agonists tested, RSQ exhibited the highest potency. As depicted in **Figure 1B**, a highly significant ($p < 0.05$), 16 ± 3.4 -fold increased TNF- α expression was observed with RSQ treatment at 1 μ M concentration, whereas IMQ exhibited moderated increase (3 ± 0.32 -fold), and with PTX, only basal level of expression was observed (0.3 ± 0.2 fold). Even at a lower concentration of 500 nM, RSQ exhibited an 8 ± 1.8 -fold increase in TNF- α expression, signifying greater potency of RSQ. Based on these observations, RSQ was selected as the candidate TLR-agonist to be used with PTX for combined chemo-immunotherapy.

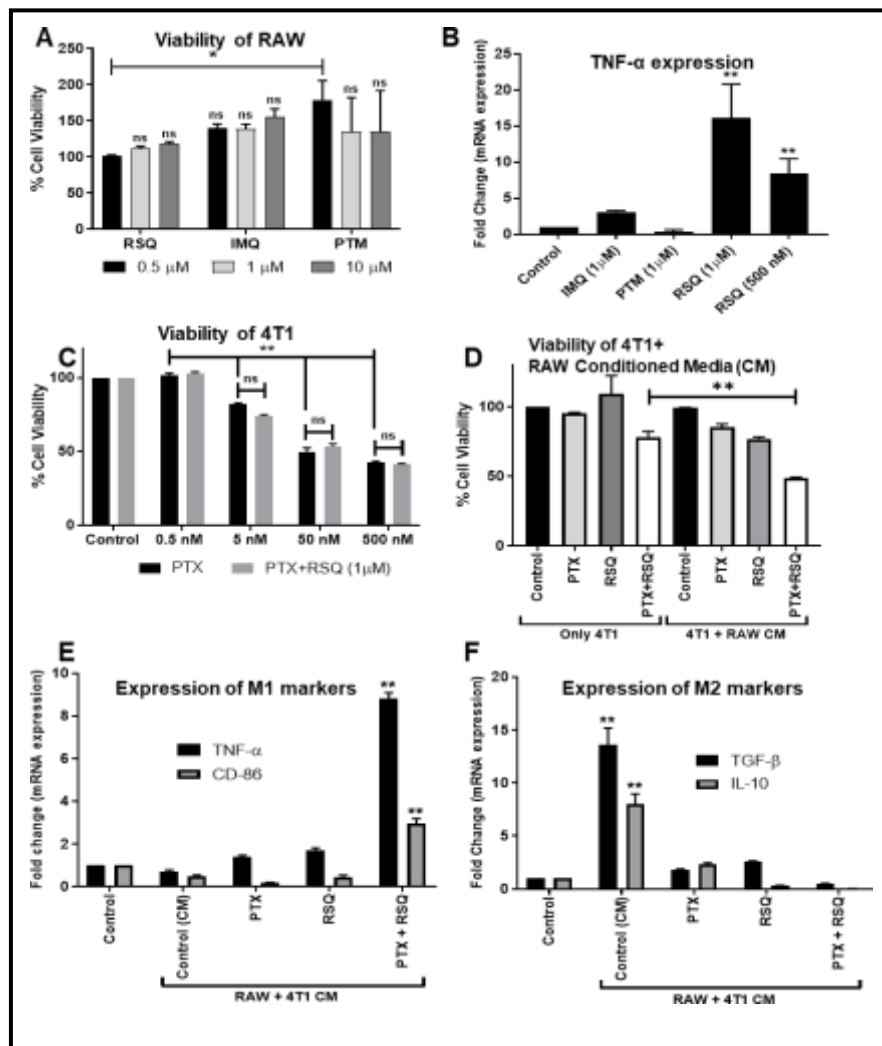


Figure 1: A. Evaluation of the cytotoxicity of different TLR agonists on RAW 264.7 cells. B. Evaluation of the macrophage stimulatory activity of different TLR agonists. C. Evaluation of the effect of RSQ (1 μ M dose) treatment on the cytotoxic activity of PTX on 4T1 cancer cells. D. Analysis of the combined efficacy of PTX+RSQ treatment in a quasi-co culture experiment using 4T1 cancer cells and conditioned medium of RAW 264.7 macrophages. E. Analysis of the expression of M1 markers by RAW 264.7 macrophages exposed to a conditioned medium of 4T1 cancer cells treated with different drugs. F. Analysis of the expression of M2 markers by RAW 264.7 macrophages exposed to conditioned medium of 4T1 cancer cells treated with different drugs. ** indicates $p < 0.05$.

Evaluation of combined chemo-immunotherapeutic efficacy:

Immunotherapy can be combined with chemotherapy to improve its efficacy. PTX was selected as a model drug for combined chemo-immunotherapy and RSQ as the immune modulator. To determine whether RSQ treatment can directly influence the activity of PTX, 4T1 cancer cell viability was evaluated when treated with PTX alone and PTX+RSQ combination. As shown in **Figure 1C**, dose-dependent cytotoxicity was observed for PTX treatment (in 0.5 to 500 nM range); however, the inclusion of RSQ at 1 μ M dose did not significantly influence the cytotoxic potential of PTX, indicating no synergistic or additive effect of this drug combination

against cancer cell alone. Next, to find out the chemo-immunotherapeutic efficacy of PTX+RSQ combination, initially, RAW 264.7 cells were treated with PTX alone (5 nM) or RSQ alone (1 μ M) or PTX+RSQ combination for 24h. After 24h, the conditioned medium was added to 4T1 cells and incubated for 48h. 4T1 cells directly treated with PTX alone (5 nM), RSQ alone (1 μ M), or PTX+RSQ combination for 48h were taken as controls to compare the efficacy of RAW 264.7 cells conditioned medium with drug treatments. Direct treatment on the 4T1 cells was found to have low cytotoxicity, with RSQ exhibiting no cytotoxicity, and PTX and PTX+RSQ showed $90\pm2.3\%$ and $72\pm3.4\%$ cell viability, respectively (**Figure 1D**). Treatment of the 4T1 cells with the RAW 264.7 conditioned medium with PTX or RSQ alone exhibited similar cytotoxicity ($85\pm1.6\%$ and $77\pm1.4\%$ viability, respectively). Interestingly, treatment of the 4T1 cells with RAW 267.4 conditioned medium with PTX+RSQ combination exhibited significantly increased cancer cell death ($49\pm1.2\%$ viability, **Figure 1D**). This data signifies the improved chemo-immunotherapeutic efficacy of the PTX+RSQ combination.

Next, the immunomodulatory potential of this drug combination was evaluated. 4T1 cells (50,000 cells/ well in a 6 well plate) were treated with PTX alone (5 nM), or RSQ alone (1 μ M), or PTX+RSQ combination for 24h, and the conditioned medium was transferred to RAW 264.7 cells. After 24h incubation with the conditioned medium, the expression of M1 (TNF- α , CD86) and M2 (IL10, CD206) markers were analyzed using qRT-PCR. Treatment of RAW264.7 with the native 4T1 conditioned medium was found to polarize the RAW 264.7 cells to an M2 phenotype with a significant increase in TGF- β (13 ± 2.4 -fold) and IL10 (8 ± 1.3 -fold) expression, whereas expression of M1 markers TNF- α and CD86 was at a basal level. However, treatment of the 4T1 cells with both PTX and RSQ alone abolished the M2 polarizing activity of the conditioned medium and restored the macrophages. Remarkably, treatment with PTX+RSQ combination to the 4T1 cancer cells normalized the M2 marker expression to the basal level and significantly increased the M1 marker TNF- α (9 ± 0.5 -fold) and CD86 (3 ± 0.4 -fold), indicating polarization of the macrophages to the immune stimulatory M1 phenotype.

Synthesis and characterization of the pH-sensitive polymer

After establishing improved chemo-immunotherapeutic efficacy of the PTX+RSQ combination, a pH-sensitive NP delivery system was developed for TME-targeted delivery of the drug combination. A five-armed star-shaped PLGA was modified by conjugating it with poly-(L-Histidine) as a pH-sensitive moiety at the end of each arm. This modified polymer should remain in the non-polar, unionized form in the systemic circulation at neutral pH,

protecting the drug in encapsulated form. However, upon reaching the TME, it would get destabilized due to protonation of histidine groups at the acidic pH and converted to ionic form, leading to a quick release of the entrapped drugs. The reaction scheme is depicted in **Scheme 1**. Initially, the terminal hydroxyl group of a commercially available star-shaped PLGA (s-PLGA-OH) was converted to the carboxyl (s-PLGA-COOH) by reacting with succinic anhydride. In a separate reaction, Boc-His (DNP)-OH was reacted with thionyl chloride in DMF to form DNP-NCA-HCl, then reacted with iso-propylamine for ring-opening polymerization and production of poly-(N-DNP-L-Histidine). Then poly-(N-DNP-L-Histidine) was reacted with the previously formed s-PLGA-COOH to form s-PLGA-poly-Histidine-DNP in the presence of EDC and NHS. After every step, the product was purified by precipitation in ice-cold DEE and dried under a vacuum. DNP deprotection was done by using 50% 2-mercaptoethanol. The final product was dialyzed against distilled water to remove byproducts if formed. It was then lyophilized, and the final yield was around 92%. It was then stored at -20°C for further use. A linear PLGA (l-PLGA) was similarly modified to compare the polymer's shape to the pH-sensitive behavior. Poly-(N-DNP-L-Histidine) was reacted with l-PLGA-COOH in the presence of EDC and NHS and was purified with ice-cold DEE and dried under vacuum followed by DNP deprotection.

The final product obtained was characterized using ^1H NMR (**Figure 2**). Herein, Boc-His(DNP)OH has shown a peak at δ h12.6 ppm [which is of -COOH group of histidine, at δ 7.9, 8.63, and 8.68 ppm [which belonged to the DNP group (i1, i2, and i3)], and at δ j1.36 ppm [that corresponds to the Boc group]²³. The ^1H NMR spectrum (in DMSO- d_6) of NCA showed peaks at δ 8.2–9 ppm (the proton b, c, and d on phenyl group, DNP), δ a 9.2 ppm (-N=CH-C), δ e 7.9 ppm (-N=CH-N), δ f 4.9 ppm (-CH-) and δ g 3.20 ppm (-CH₂) (Figure-2). The ^1H NMR spectrum (DMSO- d_6) of poly-(Nim-L-histidine) has not shown peaks at δ 8.15–9.00 ppm (proton a, c, and d on phenyl group, DNP), which indicates the successful deprotection of DNP, δ b 8.4 ppm (-N=CH-C), δ e 7.4 ppm (-N=CH-N), δ f 3.9 ppm (-CH-), δ g 3.7 ppm (-CH₂) and δ h 1.4 ppm (-C(CH₃)₂).²³

s-PLGA has shown peaks at δ a 5.32, δ b 4.81, and δ c 1.7 ppm, which were also present in the final product, s-PLGA-pH.s-PLGA-pH showed peaks at δ f1.2 ppm ((-C(CH₃)₂)), δ 7.3 ppm (-N=CH-N), δ 3.9 ppm (-CH-), and δ d 3.6 ppm (-CH₂), which all are indicative of the histidine group. However, the peaks at δ 8.25–9.1 ppm (the proton on phenyl group, DNP) were absent, signifying the removal of the DNP moiety. Overall, the NMR spectrum established the successful formation of histidine conjugated s-PLGA-pH.

Similarly, ^1H NMR of l-PLGA revealed characteristic peaks at δ_a 1.6 ppm ($-\text{CH}_3$), δ_c 4.97 ppm ($-\text{CH}_2-$), and δ_b 5.23 ppm ($-\text{CH}-$).²⁴ l-PLGA-pH has shown the peaks similar to PLGA at δ_a 1.9 ppm ($-\text{CH}_3$), δ_c 4.99 ppm ($-\text{CH}_2-$), and δ_b 5.18 ppm ($-\text{CH}-$), along with δ_d 1.5 ppm ($(-\text{C}(\text{CH}_3)_2)$), δ 7.24 ppm ($-\text{N}=\text{CH}-\text{N}$), δ 3.9 ppm ($-\text{CH}-$), δ_e 3.6 ppm ($-\text{CH}_2$) of histidine group indicates the successful formation of histidine conjugated l-PLGA-pH.

Further FTIR analysis was carried out to confirm the successful conjugation of poly-histidine to s-PLGA (**Figure 3**). The absence of OH peak and presence of N-C=O peak has shown the DNP-NCA-HCl formation; after that, the presence of N-H and C=O has proved the formation of poly-(N-DNP-L-Histidine). In the FTIR spectra of s-PLGA-pH, the absence of -OH stretch (at $\sim 3200\text{ cm}^{-1}$) indicated ester link formation between poly-histidine and s-PLGA. Along with the absence of the -OH group signal, s-PLGA-pH also exhibited NH (3400 cm^{-1}), stretching vibrations of histidine and C=O (1750 cm^{-1}), C-O (1100 cm^{-1}) stretching vibrations, and CN stretch (1089 cm^{-1}) of s-PLGA. Even with l-PLGA, the absence of O-H and the presence of C-N has shown the product formation of l-PLGA-pH. Altogether, ^1H NMR and FTIR results confirmed the successful formation of s-PLGA-pH and l-PLGA-pH.

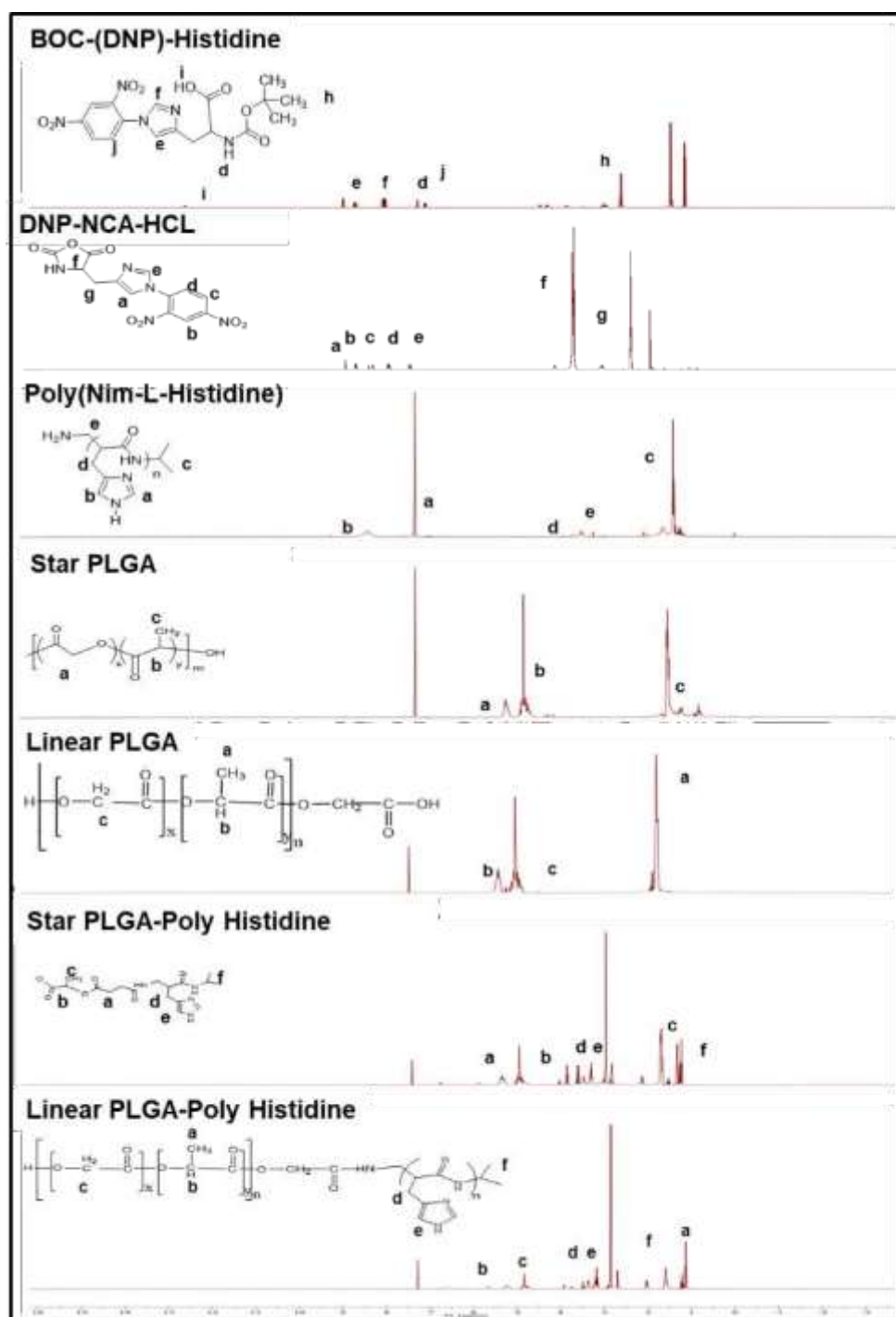


Figure 2: Structural characterization of the modified polymers using NMR spectroscopy.

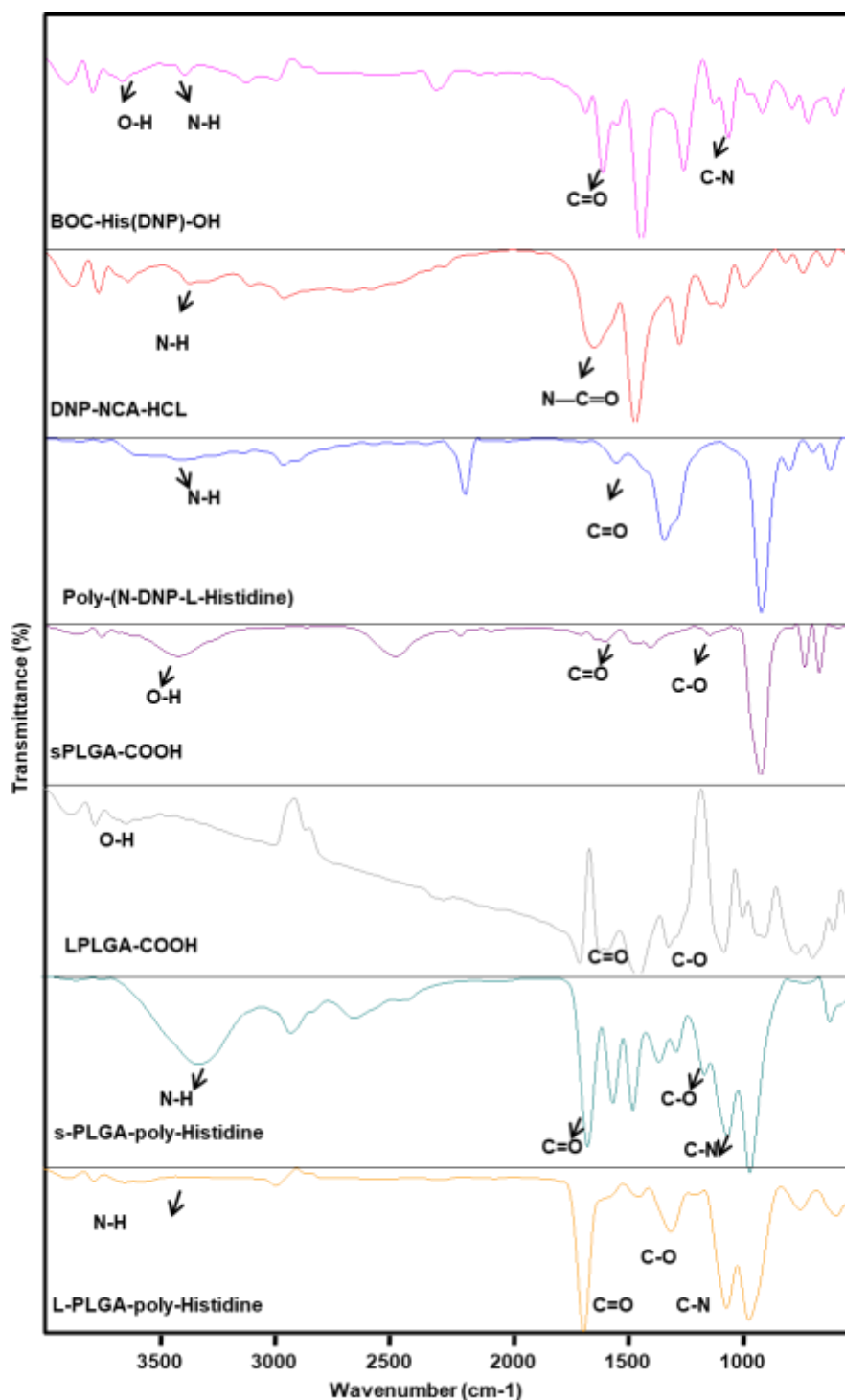


Figure 3: Structural characterization of the modified polymers using FT-IR spectroscopy.

Preparation and characterization of PTX and RSQ loaded nanoparticles

The microfluidic-based nanoprecipitation method was used to prepare the drug-loaded NPs using these pH-sensitive polymers. Both the drugs (PTX and RSQ [100μg and 2mg] were

dissolved in ACN(1mL) containing 20 mg of the polymer. 0.5 % Soluplus (BASF Pharma) was used as a stabilizer in the aqueous phase (10mL). Both the phases (organic and aqueous) were injected into a micromixer chip with the help of a syringe pump. The aqueous to organic flow rate was optimized to 1:10 ratio (organic 10 μ L/min and aqueous 100 μ L/min). Hydrodynamic flow focusing and turbulent mixing in the Herringbone mixture allowed for the rapid exchange of solvent, resulting in the drug-loaded NP formation. The resultant NP suspension was kept for overnight stirring at room temperature for solvent evaporation; then, it was dialyzed against distilled water to remove the organic solvent and un-entrapped drugs.

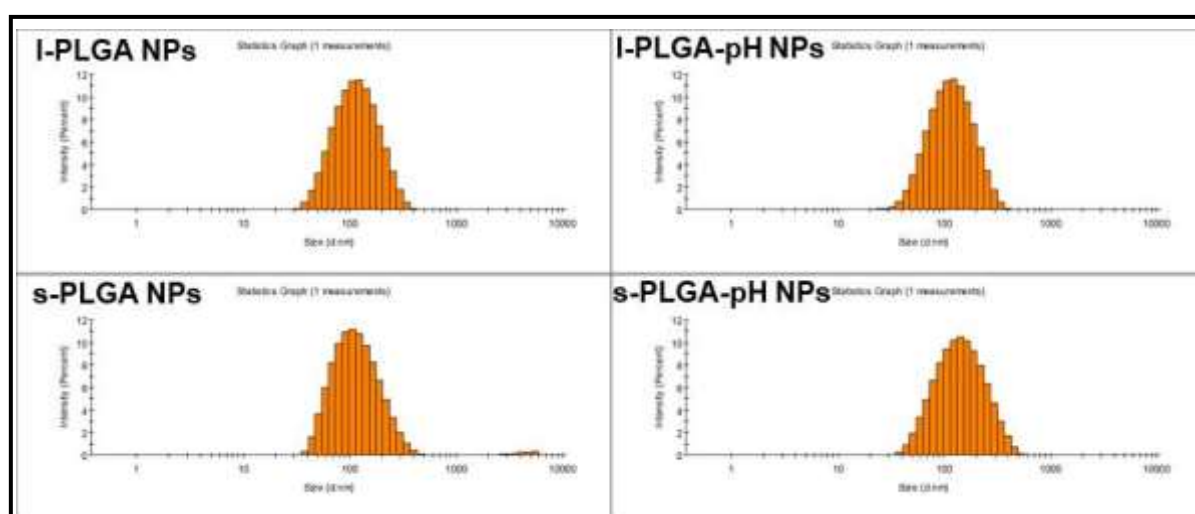


Figure 4: Particle size analysis of different NPs prepared with different polymers.

Table 1: Effect of polymer modification on physicochemical characteristics of NPs

Type	Size (nm)	PDI	EE (%)	LC (%)
s-PLGA NPs	120 \pm 5.2	0.29 \pm 0.03	74 \pm 0.12% PTX, 69 \pm 0.61% RSQ	10.5 \pm 0.16%
s-PLGA-pH NPs	128 \pm 2.6	0.24 \pm 0.12	80 \pm 0.86% PTX, 85 \pm 0.32% RSQ	9.83 \pm 0.25%
I-PLGA NPs	121 \pm 3.5	0.31 \pm 0.02	69 \pm 0.18% PTX, 64 \pm 0.36% RSQ	9.61 \pm 0.12%
I-PLGA-pH NPs	136 \pm 3.2	0.28 \pm 0.10	70 \pm 0.21% PTX, 87 \pm 0.32% RSQ	8.57 \pm 0.27%

The same procedure was followed with all four polymers (I-PLGA, s-PLGA, I-PLGA-pH, and s-PLGA-pH) with similar amounts of drug, polymer, and stabilizer concentration to make NPs, and the particle size was analyzed. Uniform particle sizes and PDIs were observed with NPs

prepared with all the polymers (**Figure 4** and **Table 1**). The size was around 100-120nm, with a PDI of around 0.1-0.4. The Zeta potential of all the four different NPs was found to be in the range of -6 to -8 (**Table 1**). Next, the entrapment efficiency and drug loading of PTX and RSQ were checked, as described in **Table 1**. All the NPs exhibited high entrapment efficiency and drug loading; however, moderately increased encapsulation was observed with the 5-armedPLGA (s-PLGA) over the linear PLGA (l-PLGA) and after poly-histidine modification.

Next, the pH-dependent stability of all the formulations (s-PLGA, l-PLGA, s-PLGA-pH, and l-PLGA-pH) was compared at two different pH: 7.4 and 6.5. First, pH-dependent change in the particle size was evaluated with the help of DLS. As depicted in **Figure 5A**, no significant change in size was observed in the l-PLGA and s-PLGA NPs at both pH levels, even after 6h of incubation. l-PLGA NPs had shown size of 212 ± 1.7 nm in pH 7.4 and 191 ± 2.3 in pH 6.5. s-PLGA NPs exhibited a size of 174 ± 2.5 nm in pH 7.4 and 131 ± 3.6 nm in pH 6.5. In both cases, PDI was between 0.1-0.3. On the other hand, both the pH-sensitive NPs exhibited pH-dependent size variation. l-PLGA-pH and s-PLGA-pH NPs remained stable at pH 7.4 (169 ± 5.3 nm and 195 ± 6.2 nm, respectively) with a PDI of 0.1-0.3. However, at pH 6.5, a significant change in size happened. The size of l-PLGA-pH NPs was 2420 ± 522.1 nm, and s-PLGA-pH NPs were 8184 ± 857.2 nm, with a PDI of 1, indicating high polydispersity (**Table 2**).

Table 2: Effect of pH on the size and PDI of the NPs measured using DLS (n = 3).

NP formulations	pH 7.4				pH 6.5			
	0h		6h		0h		6h	
	Size	PDI	Size	PDI	Size	PDI	Size	PDI
I-PLGA	176 ± 3.1	0.2	212 ± 1.7	0.3	109 ± 2.4	0.2	191 ± 2.3	0.2
I-PLGA-pH	98 ± 2.4	0.2	169 ± 5.3	0.2	280 ± 2.3	0.3	2420 ± 2.1	1
s-PLGA	164 ± 4.1	0.2	174 ± 2.5	0.1	101 ± 3.7	0.3	131 ± 3.6	0.1
s-PLGA-pH	112 ± 1.3	0.3	195 ± 6.2	0.2	308 ± 2.7	0.4	8184 ± 8.2	1

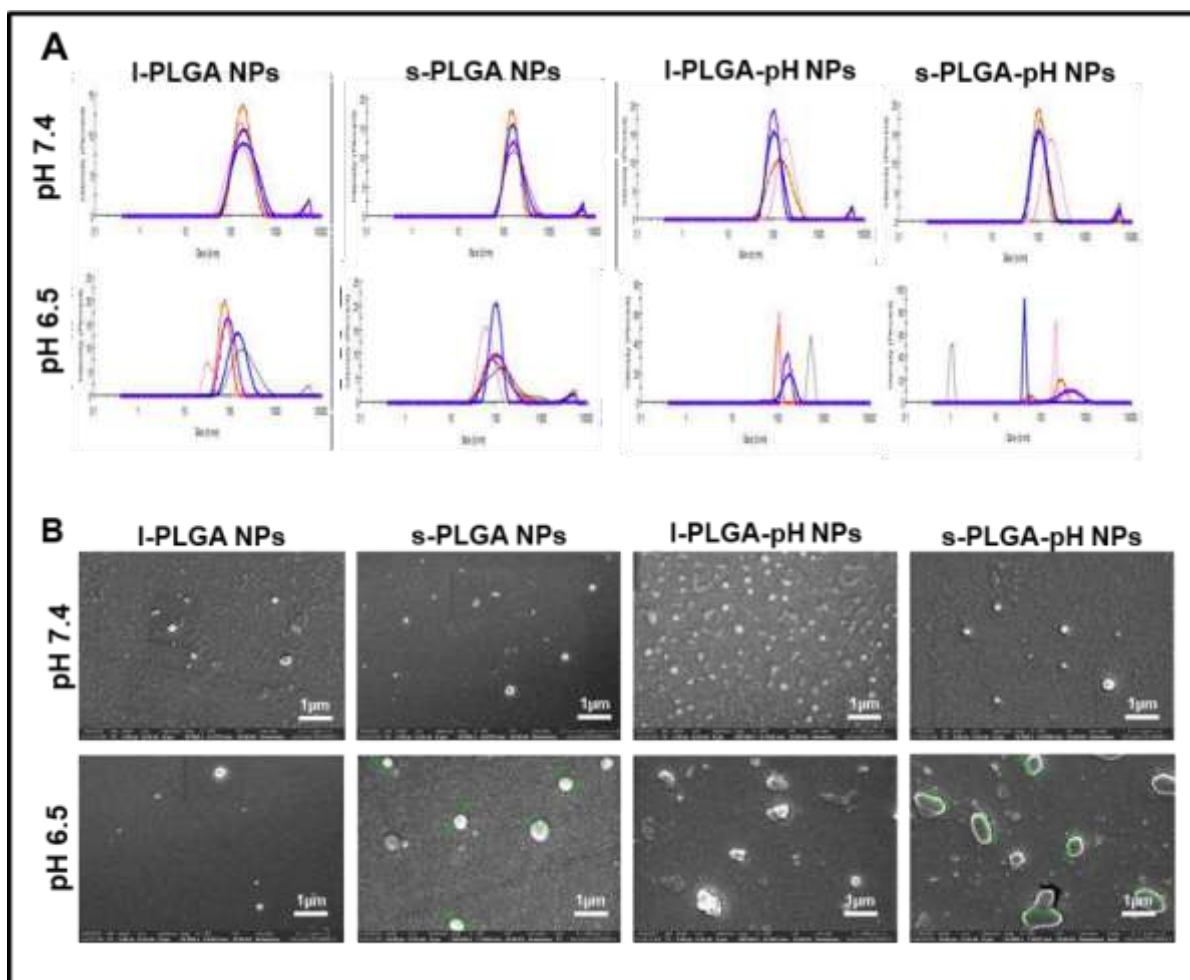


Figure 5: A. Particle size analysis through DLS of different NPs incubated at different pH (7.4 and 6.5) for 6h. B. SEM analysis of the size and shape of the NPs incubated at different pH (7.4 and 6.5).

Then, the pH-dependent change in particle size was evaluated by field emission scanning electron microscopy (FE-SEM) for further confirmation. Corroborating with the DLS data, I-PLGA and s-PLGA NPs were similar in size and morphology at pH 7.4 and 6.5 after 3h incubation (**Figure 5B**). In contrast, a significant change in the size and morphology was observed with the I-PLGA-pH and s-PLGA-pH NPs at pH 6.5 after 3h incubation, compared to NPs incubated at pH 7.4.

***In-vitro* drug release**

To evaluate the effect of pH on the drug release pattern, an *in-vitro* cumulative drug release study of drug-loaded (PTX and RSQ) NPs prepared with different polymers incubated at different pH (7.4, 6.5, and 5.5) was performed. I-PLGA, compared to s-PLGA, was more sensitive to changes in the pH. The cumulative drug release after 72h from I-PLGA NPs was found to be $55 \pm 4.3\%$ for PTX and $39 \pm 1.6\%$ for RSQ in 5.5 pH buffer, while $26 \pm 3.5\%$ PTX and $17 \pm 0.8\%$ RSQ were released in 7.4 pH buffer (**Figure 6A**), an increase of more than 20% in

both of the drug released at pH 5.5 compared to pH 7.4. Contrarily, s-PLGA NPs were found to be more stable, with $52\pm3.3\%$ PTX and $49\pm4.8\%$ RSQ released in 5.5 pH buffer, whereas $42\pm2.4\%$ PTX and $39\pm3.6\%$ RSQ was released in pH7.4 buffer (**Figure 6B**), a difference of about 10%. However, with poly-His modification, both the polymers exhibited significantly increased drug release at acidic pH. I-PLGA-pH NPs exhibited $79\pm3.8\%$ PTX release and $88\pm4.6\%$ RSQ release at pH 5.5, compared to $64\pm4.5\%$ PTX and $43\pm5.17\%$ RSQ release at pH 7.4 (**Figure 6C**). s-PLGA-pH NPs had shown even higher drug release at pH 5.5, which was $91\pm2.3\%$ for PTX and $92\pm5.6\%$ for RSQ, compared to $54\pm3.2\%$ PTX and $51\pm3.4\%$ RSQ release at pH 7.4 (**Figure 6D**). Interestingly, for s-PLGA-pH NPs, the drug release pattern showed almost 1:1 % release of PTX and RSQ. As our initial data indicated, maintaining this drug ratio might be necessary for improved synergistic efficacy.

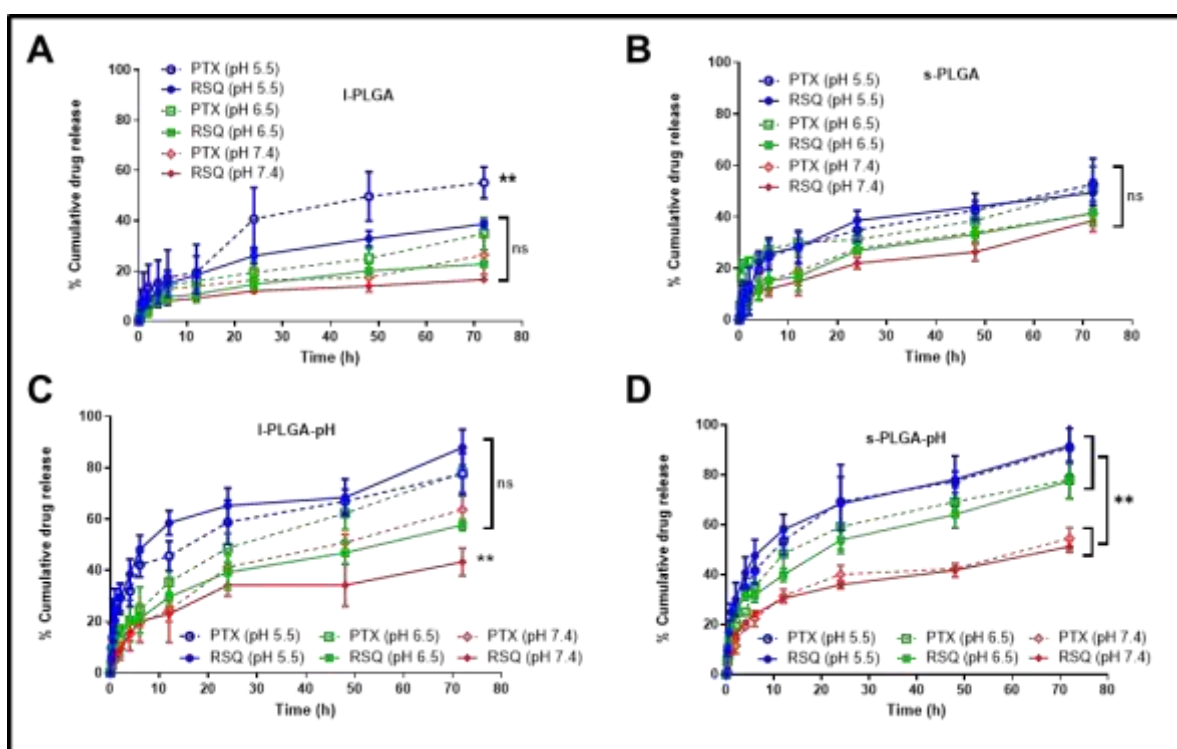


Figure 6: Cumulative drug release study from NPs prepared with different polymers.

Cytotoxicity analysis

After demonstrating the pH-sensitive property of the poly-His modified NPs, the effect of NP encapsulation of the drugs on the direct cytotoxic activity was evaluated. Both 4T1 cancer and RAW 264.7 macrophage cells were separately treated with the native drugs, their combination, and the drug combination encapsulated in the poly-His modified NPs at the dose of 5nMPTX and 1 μ MRSQ. Against only 4T1 cells, treatment with the drugs alone or in combination (both native and NP encapsulated) exhibited moderate cytotoxicity. Cell viability was found to be

75±2.3% with PTX alone, 86±1.1% with RSQ alone, and 74±2.3% with PTX+RSQ. With l-PLGA-pH NPs, cell viability was 74±1.6%, and with s-PLGA-pH NPs, it was 71±3.1% (**Figure 7A**). Against only RAW 264.7 cells, all drug treatments showed very low cytotoxicity, with more than 95% cell viability observed with all the treatments (**Figure 7B**).

Next, the cytotoxic potency of the drug combination against the co-culture of the 4T1 cancer cells and RAW 264.7 macrophage cells was evaluated. Initially, a complex cancer spheroid model, prepared with both 4T1 and RAW 264.7 cells, was developed to mimic the TME in an *in-vitro* system (**Figure 7C**). These spheroids were treated with free drugs, and NP encapsulated drugs at the dose of 10nM PTX and 2µM RSQ for 72 h. The dose of drugs was doubled for cancer spheroid treatment compared to monolayer culture because the cancer spheroids exhibit more resistance.²⁵ Cell viability was measured by MTT assay. As depicted in **Figure 7D**, treatment with PTX and RSQ alone resulted in marginal cell death, with 76±2.3% and 81±3.8% cell viability with PTX and RSQ, respectively. However, a significantly increased cell death was observed in the drug combination group. Cell viability was found to be 51±2.6% with PTX+RSQ combination treatment. This data indicated that treatment with the drug combination could have synergistic efficacy. Interestingly, encapsulation of PTX+RSQ in the pH-sensitive NPs exhibited a differential effect. With the l-PLGA-pH NPs, the cell viability was 58±5.5%, whereas, with s-PLGA-pHNPs, the cell viability was 29±3.6%. The significantly higher ($p<0.05$) cell death with the s-PLGA-pH NPs could be due to the more uniform (maintaining 1:1 ratio of PTX and RSQ, as shown in **Figure 6D**) drug release observed in the s-PLGA-pH NPs.

The mixed cancer spheroid model can mimic the actual *in-vivo* cancer more consistently. However, analyzing the death of individual cell types is challenging in that model. A transwell-based co-culture experiment was performed to understand the impact of the combination treatment on both 4T1 cancer cells and the RAW macrophages individually. In this experiment, cancer spheroids were made using 4T1 cancer cells, which were kept in the lower chamber of the trans-well, whereas RAW 264.7 cells were plated in the upper chamber (**Figure 7E**). Drug treatment was given in the lower chamber; however, as the RAW 264.7 cells are exposed in the same medium, they are equally exposed to the drug. Corroborating the observation in the experiment using the mixed cancer spheroid model, increased cancer cell death was observed with the PTX+RSQ combination treatment (38±1.5% viability). The death of the macrophages was relatively low (68±5.3% viability). Among the NP encapsulated drug treatment, treatment with s-PLGA-pH NPs exhibited increased cancer cell death (29±5.6% viability) compared to

l-PLGA-pH NPs ($46 \pm 3.5\%$ viability) (**Figure 7F**), supporting the observation in the previous experiment with mixed cancer spheroid model.

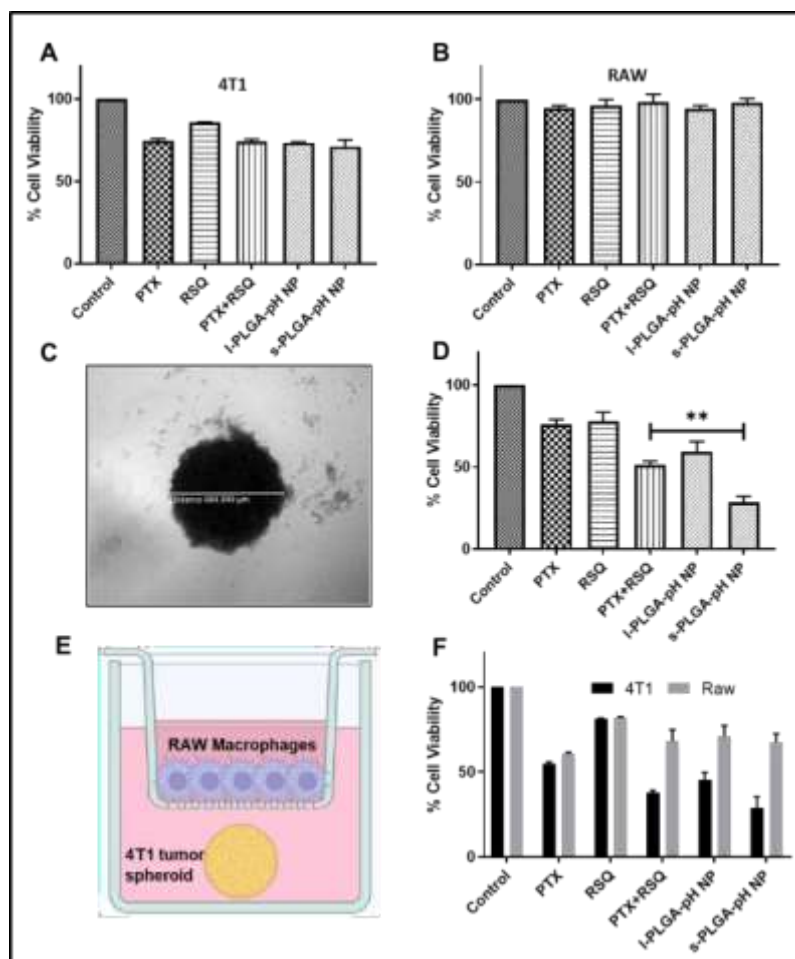


Figure 7: **A.** Direct cytotoxic activity of the drug-loaded NPs against 4T1 cancer cells. **B.** Direct cytotoxic activity of the drug-loaded NPs against RAW 264.7 macrophage cells. **C.** Microscopic image of a complex spheroid made with 4T1 cancer and RAW264.7 macrophage cells. **D.** Cytotoxic activity of the drug-loaded NPs against the complex spheroid model. **E.** Designing of a quasi-3D-coculture system to analyze differential death of cancer cells and macrophages. **F.** Analysis of cell viability of 4T1 cancer and RAW 264.7 macrophages in the quasi-3D co-culture experiment. ** indicates $p < 0.05$.

Live/dead staining

To confirm the tumor-specific death from the data we have observed with cytotoxicity data, we have performed live-dead staining. Here we have made spheroids of tumor cells (4T1) and allowed them to grow in the lower chamber of the Transwell and macrophage 2D on the transwell polycarbonate membrane in the upper chamber. All the treatment groups, i.e., PTX, RSQ, PTX +RSQ, SP NPs, and spH NPs (s-PLGA-pH NPs), were exposed for 72h and then followed by Annexin, PI staining, thereafter the fluorescent images were captured for both 4T1 spheroids and 2D macrophages along with shape and morphology.

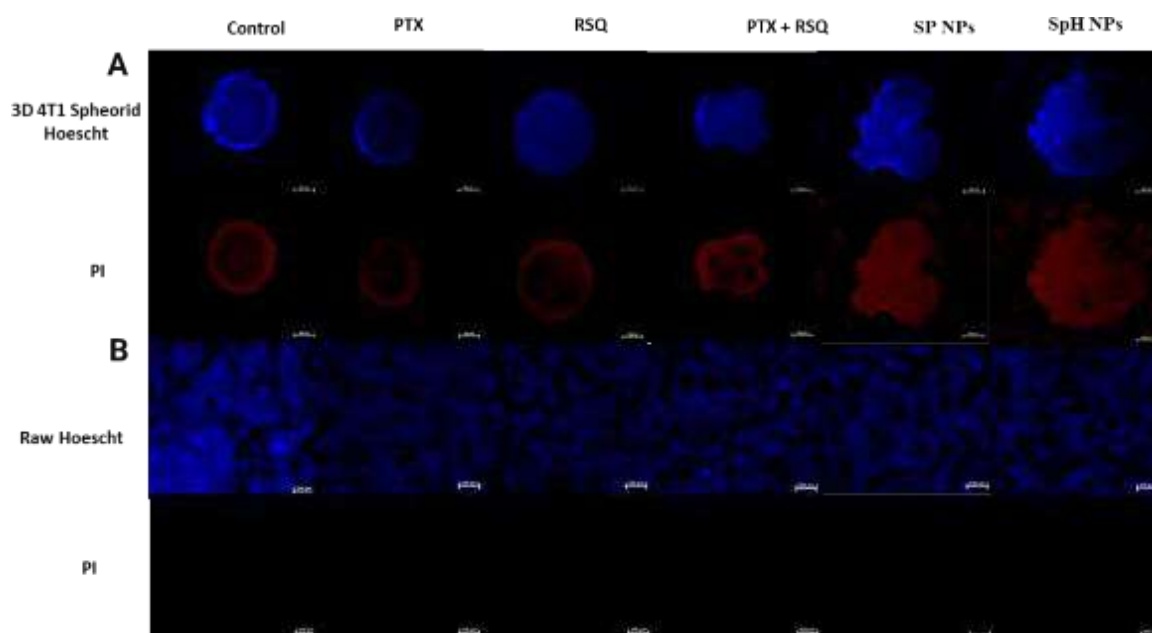


Figure 8: Live/dead staining in transwell system of 4T1 tumor and 2D raw 264.7 cells. **A)** Representative fluorescent images of 4T1 tumor spheroids used for the analysis of cell death stained with Propidium iodide (PI) and Hoechst 33342 as outlined. **B)** Representative fluorescent images of 2D RAW 264.7 cells for the analysis of cell death stained with Propidium iodide (PI) and Hoechst 33342. Scale bars indicate 100 μm.

In **figure 8**, after 72h of the treatment period, we can see that the shape of the spheroids of control and free drugs are stable till 72h, which were conversely deformed with combination treatment and NPs; this might be because of the cytotoxicity of the treatment groups.

Cancer spheroid penetration

After observing increased cell death with the s-PLGA-pH NPs compared to l-PLGA-pH NPs in the cancer spheroid model, drug penetration using these two types of pH-sensitive NPs was analyzed in the cancer spheroids using DiI-loaded NPs. Non-pH-sensitive NPs were used as a control. Here, cancer spheroids were treated with DiI-loaded l-PLGA, s-PLGA, l-PLGA-pH, and s-PLGA-pH NPs and were observed under the microscope after 24h.

As depicted in **Figure 9A**, a significant difference in the distribution and penetration of DiI fluorescence was observed between the pH-sensitive and non-pH-sensitive NPs. With both l-PLGA and s-PLGANPs, DiI fluorescence was mainly localized in the periphery of the cancer spheroid. However, with l-PLGA-pH and s-PLGA-pH NPs, significantly increased spheroid core penetration was observed (**Figure 9B**). Among all the groups, s-PLGA-pH NPs exhibited the highest spheroid core penetration, significantly more than l-PLGA-pH NPs.

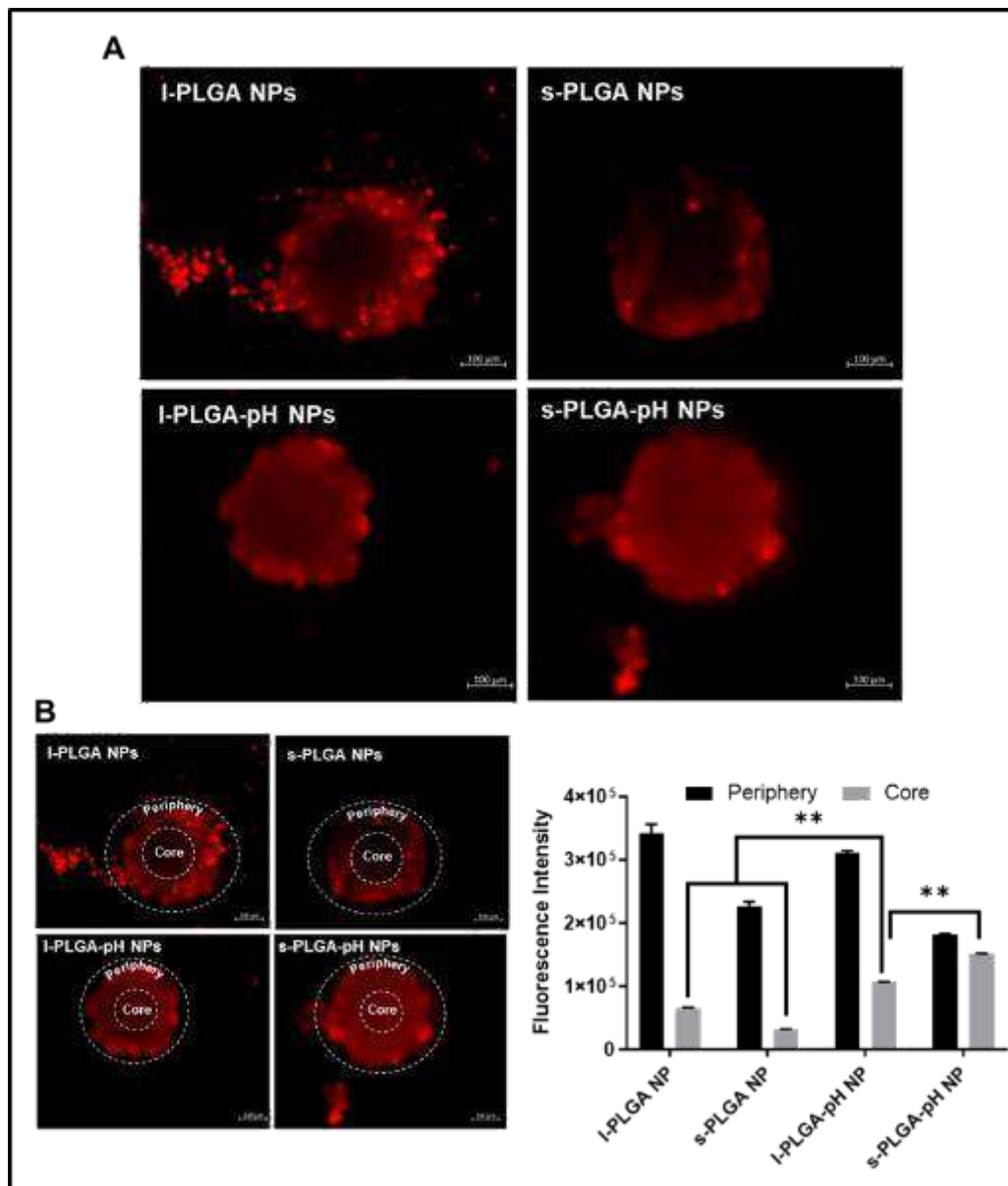


Figure 9: **A.** Cancer spheroid penetration of DiI loaded NPs was evaluated after 24 h treatment using fluorescence microscopy at 10X magnification (scale bar = 100 μ m) **B.** Quantification of fluorescence intensity in cancer spheroid core and periphery using ImageJ software. ** indicates $p < 0.05$.

Analysis of the gene expression pattern:

After confirming increased cancer cell death in the cancer spheroid model, the macrophage polarization pattern with the NP treatment was analyzed in the transwell-based mixed cancer spheroid model (as illustrated in **Figure 7E**). For that, RAW 264.7 macrophages were plated in the upper chamber of the transwell, and the cancer spheroid was placed in the lower chamber. As observed in the 4T1 conditioned medium experiment with the free drugs (**Figure 1E**), treatment with PTX+RSQ resulted in increased expression of M1-markers, TNF- α , and CD-

86, compared to the control. Interestingly, NP-encapsulated drugs exhibited higher expression of TNF- α and CD-86 compared to the free drugs (Figure 10A).

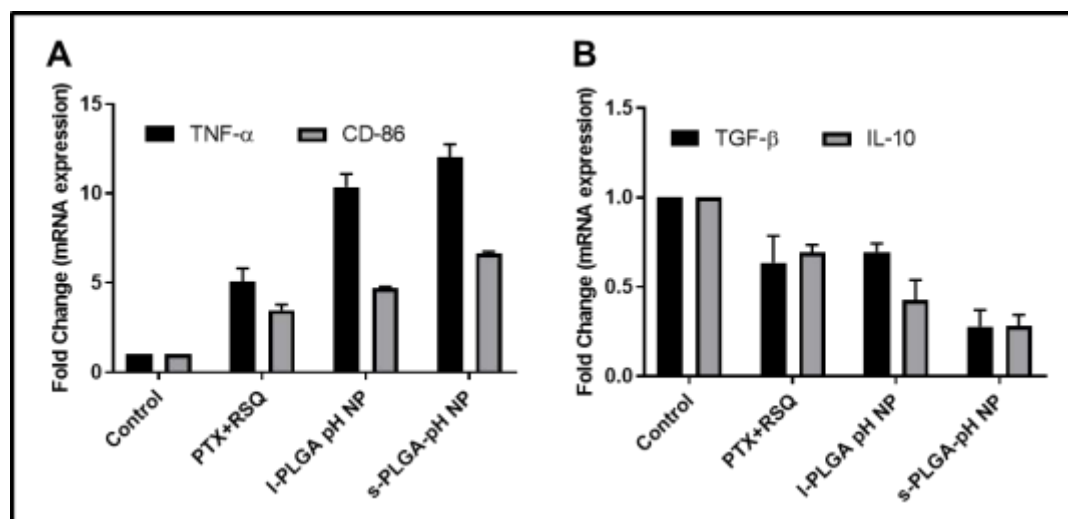


Figure 10: A. Analysis of the expression of M1 markers by RAW 264.7 macrophages in a quasi-3D co-culture experiment treated with drug combination and pH-sensitive NPs B. Analysis of the expression of M2 markers by RAW 264.7 macrophages in a quasi-3D co-culture experiment treated with drug combination and pH-sensitive NPs.

With l-PLGA-pH NPs, expression of TNF- α and CD-86 was found to be 10 ± 1.2 -fold and 5 ± 0.6 -fold, respectively, whereas with s-PLGA-pH NPs, it was 12 ± 1.3 -fold and 7 ± 0.5 -fold. Apart from increased expression of the M1-markers, M2-markers, TGF- β , and IL-10 were decreased with the PTX+RSQ treatment, both free and NP-encapsulated drugs. With the free drug treatment, expression of TGF- β and IL-10 was found to be 0.6 ± 0.1 -fold and 0.7 ± 0.06 -fold, respectively, which further decreased to 0.3 ± 0.08 -fold and 0.3 ± 0.07 -fold with the s-PLGA-pH NPs (Figure 10B). l-PLGA-pH NPs exhibited 0.7 ± 0.05 -fold expression of TGF- β and 0.4 ± 0.09 -fold expression of IL-10. This data signified the enhanced *in-vitro* immunotherapeutic ability of the PTX+RSQ drug combination encapsulated in a pH-sensitive NP.

In-vivo toxicity studies

After observing the improved *in-vitro* efficacy of this drug combination and NPs, we tested the doses for their *in-vivo* toxicity studies. During and after the treatment period, there is no significant weight variation of the animals among all the groups and no behavioral changes. Tissues were isolated after the treatment period and were sectioned, followed by H&E staining. Microscopy images of all the tissues exhibited normal structures without any signs of toxicity,

like inflammation and fibrosis (**Figure 11C**). These results show that PTX, RSQ, PTX +RSQ, and NPs are non-toxic at these doses within this period.

In-vivo pharmacokinetic studies

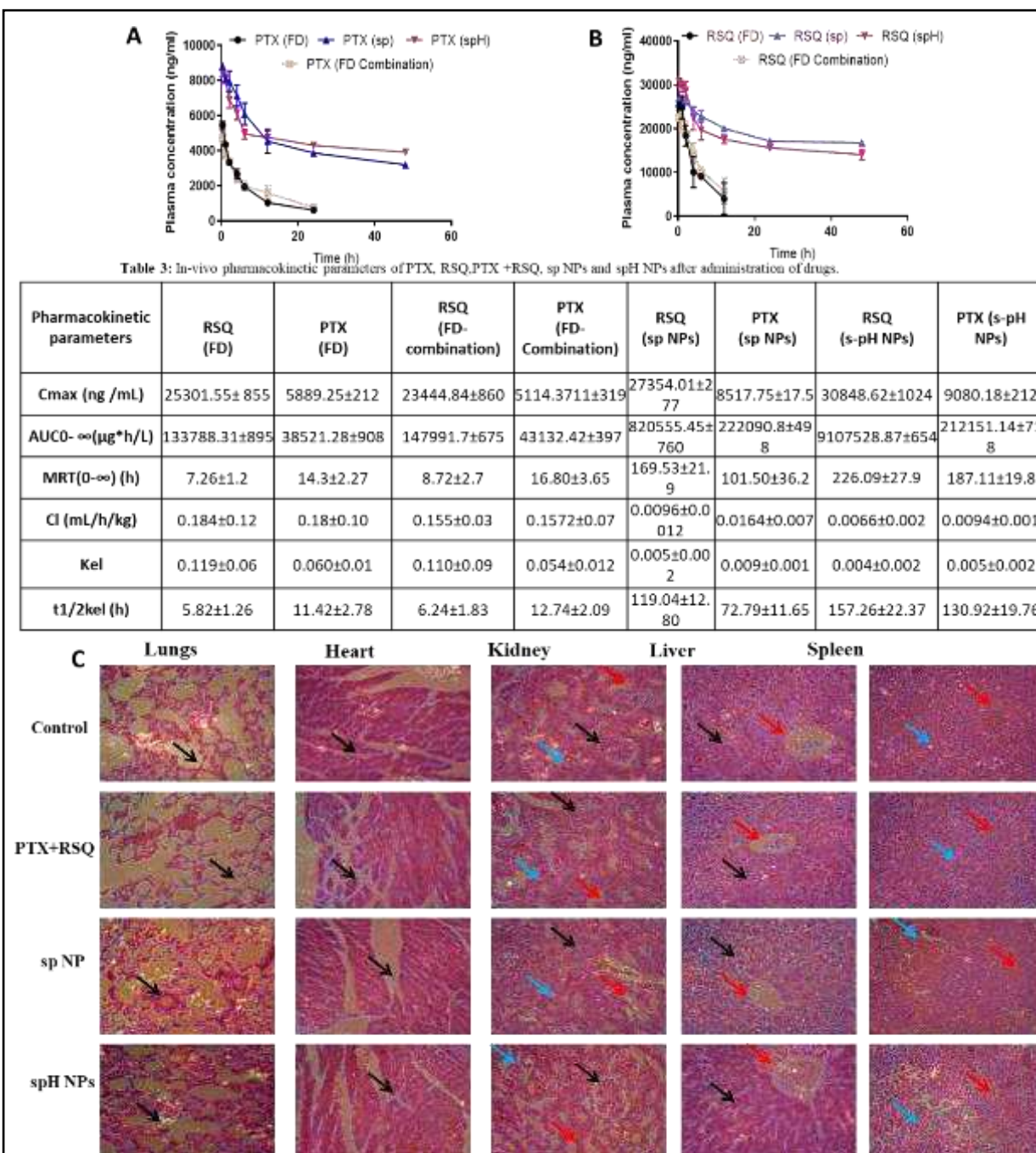


Figure-11 A. Plasma drug concentration-time profile of PTX and **B** Plasma drug concentration-time profile of RSQ. **C** Histopathological evaluation (H&E staining, 40X) of various organs for toxicity study.

After dividing the animals into different groups, they were treated with equal doses of PTX, RSQ in PTX +RSQ, and sp, and spH NPs were administered to the animals using i.v. route. Plasma was isolated from animal blood collected at different time intervals and analyzed using the HPLC method. Interestingly, results corroborated the in-vitro data with a significant difference in the PK profiles of free drugs alone and in combination with NPs (**Figure 11A, B**). Regarding the PK parameters, the plasma half-life ($t_{1/2}$) of PTX and RSQ were improved with ~2 folds when administered in combination with PTX+RSQ. Similarly, when administered as spH NPs, there was a ~ 7-fold increase in the AUC, ~11-fold reduction in the clearance (cl), and ~150-fold increase in the $t_{1/2}$, with PTX whereas, with RSQ, there was a ~ 68-fold increase in the AUC (0- ∞), ~ 16-fold reduction in cl, and a ~130- fold increase in the $t_{1/2}$ (**Table-3**).

In-vivo biodistribution study

The distribution of spH nanoparticles was evaluated using a mouse model with 4T1 tumor-bearing mice model. The behavior of these nanoparticles *in vivo* was observed over time using an imaging system. According to the data presented in Figure 10A, both sp NPs and spH nanoparticles exhibited rapid accumulation in the tumor within 15 minutes of administration. The fluorescence signal from sp NPs diminished within 1440 minutes (as indicated in **Figure 12C**) due to their interaction with plasma proteins and subsequent hepatic elimination.

Figure 12B depicts *ex vivo* fluorescence pictures of dissected tissues taken 24 h after injection. The tumor fluorescence in the spH NPs treated group is much greater than in the sp NPs group, and the spH NPs may efficiently accumulate in the tumor location. Additionally, both groups detected no significant fluorescence signals in the lungs, heart, or spleen. However, mild fluorescence signals in the kidney and liver were observed in both groups, potentially due to effective renal elimination.

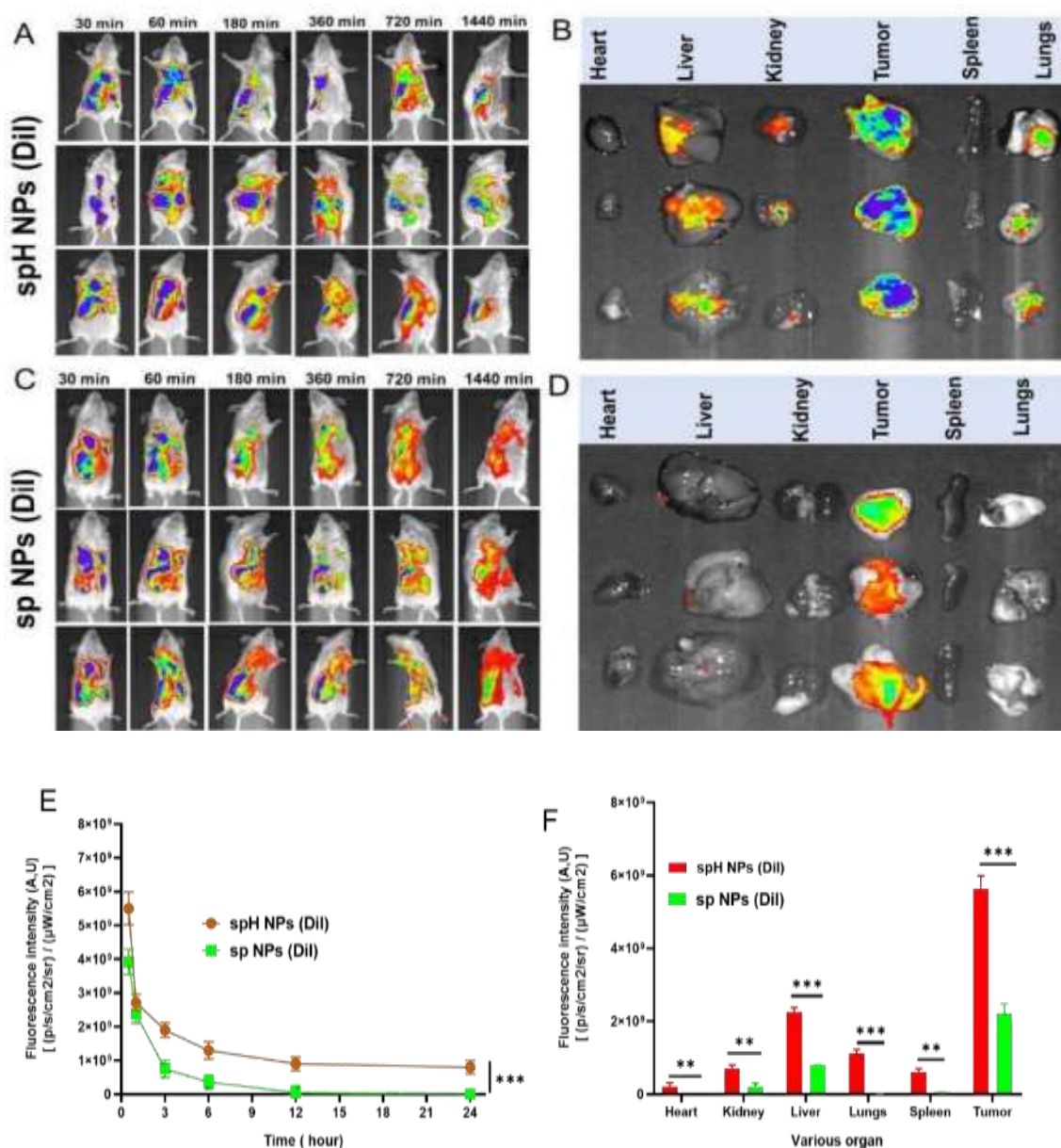


Figure 12: A & C) Fluorescent images of the whole body of the mice captured by the IVIS Lumina system at various time points (0.5, 1, 3, 6, 12, and 24 h) after DiI-encapsulated NP administration. B & D) Fluorescent images of the tumor, liver, lungs, kidney, spleen, and heart. E) Total body fluorescent intensity and time plot. F) Fluorescent intensity of different organs after isolation indicating increased tumor distribution of spH NPs (Dil) and sp NPs. (In all the panels, ** represents $p < 0.01$, *** represents $p < 0.001$, and **** represents $p < 0.0001$).

In-vivo anti-tumor efficacy study

Subsequently, the effectiveness of the nanoparticles (NPs) in inhibiting tumor growth was assessed *in vivo* using female BALB/c mice bearing 4T1-Luc tumors. The NPs were administered at the same dose that had been utilized for the toxicity study on days 0, 4, and 8. The extent of tumor growth was measured utilizing bioluminescence through luciferin-mediated detection (Figure 12A). Notably, the control group exhibited a consistent and

substantial increase in luminescence signal, signifying rapid tumor growth (**Figure 13A**). In contrast, the groups treated with the drug showed considerably diminished luminescence signals. Among all the groups, the spH NPs group demonstrated the least luminescence, significantly lower than any other group (**Figure 13B**). Apart from bioluminescence measurements, tumor volume was also determined by assessing tumor dimensions using the formula $[(\text{length} \times \text{width}^2)/2]$. After 21 days of treatment, the mean tumor volumes were $624 \pm 23 \text{ mm}^3$ for the PTX group, $510 \pm 28 \text{ mm}^3$ for the RSQ group, $310 \pm 87 \text{ mm}^3$ for the PTX+RSQ group, and $167 \pm 23 \text{ mm}^3$ for the spH NPs group (**Figure 12C**). At the end of the 21-day treatment period, tumors were extracted from the mice for assessment of their weight and histology. Tumor weight exhibited a consistent trend, with average tumor weights of $3.82 \pm 0.20 \text{ g}$ for the control group, $2.62 \pm 0.12 \text{ g}$ for the PTX group, $1.67 \pm 0.70 \text{ g}$ for the RSQ group, $1.20 \pm 0.45 \text{ g}$ for the PTX+RSQ group, and $0.32 \pm 0.12 \text{ g}$ for the spH NPs group (**Figure 12D**). Histological examination of tumor sections stained with hematoxylin and eosin (H&E) revealed the fewest viable cancer cells in the spH NPs group, followed by the PTX+RSQ group. The notable enhancement in the combined drug treatment's efficacy could potentially be attributed to synergistic effects between PTX and RSQ.

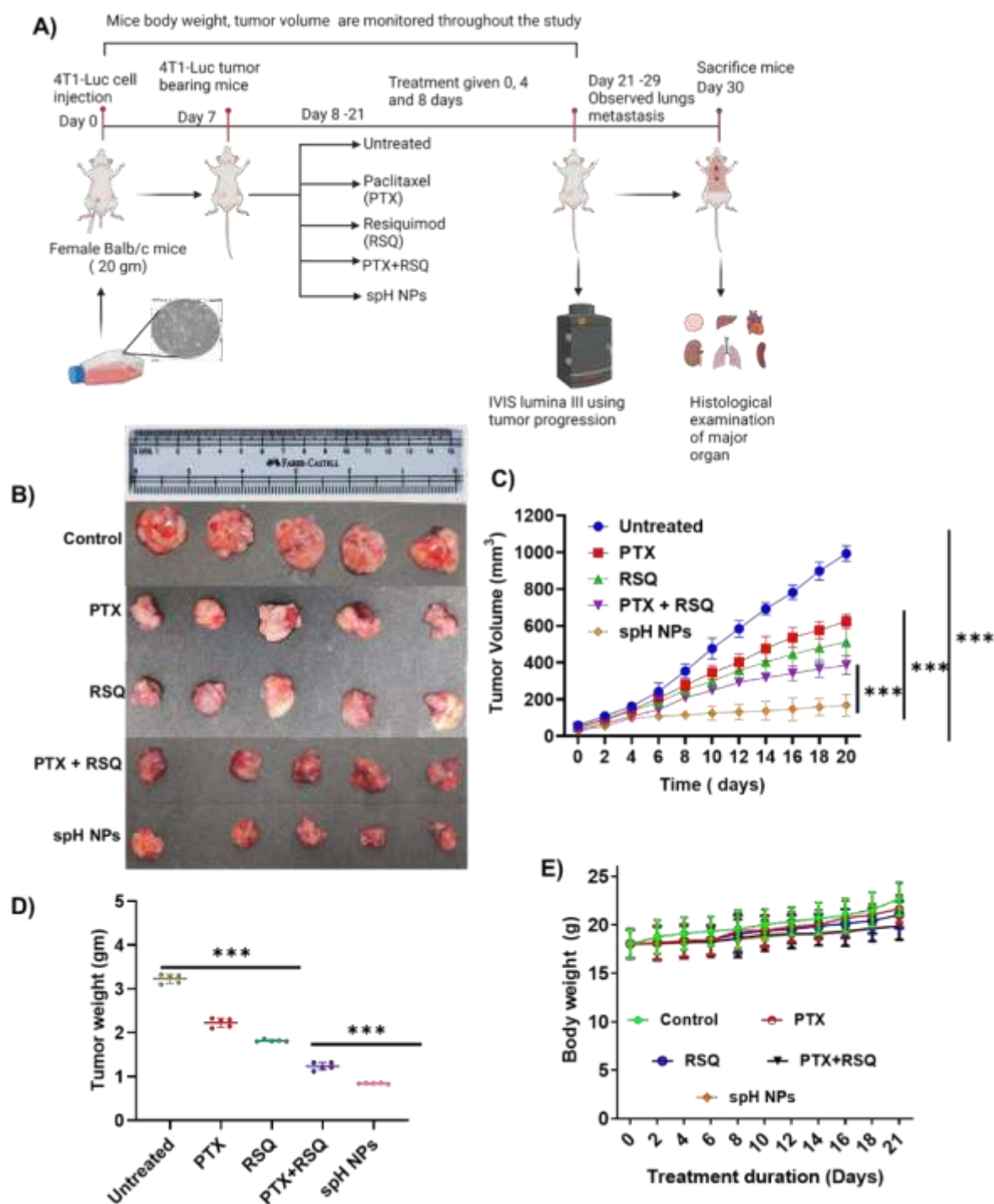


Figure 12. Anti-tumoral effect in vivo. Assessment of therapeutic Efficacy of control, PTX, RSQ, PTX+RSQ, spH NPs, in 4T1 Luc tumor-bearing C Balb/C mice. **A** in vivo dosing scheme of all formulations in B16F10 tumor bearing mice. **B** Representative appearance of tumors isolated from mice posttreatment. **C** Graphical representation of tumor volume vs. days during treatment. **D** average weight of tumors isolated from various treatment groups. **E** measurement of body weight during the treatment. *, ** and *** indicate $p < 0.05$, $p < 0.01$ and $p < 0.001$ respectively. Data represent as mean \pm SD, where $n = 5$.

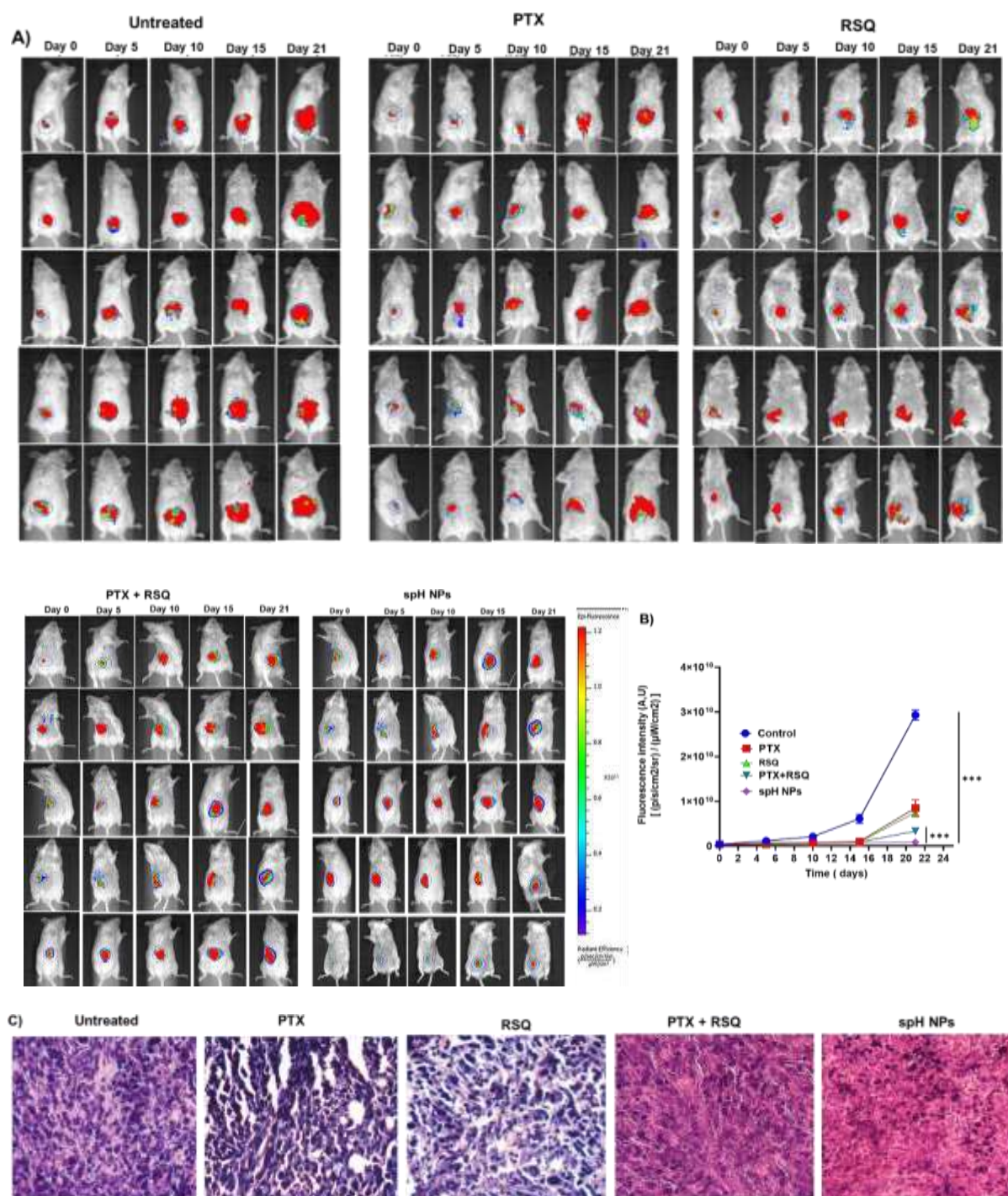


Figure 13. **A** Evaluation of the tumor growth by whole animal bioluminescence imaging of the 4T1-Luc tumors. **B** Quantification of bioluminescence of the whole animal **C** H&E-stained images of tumors. (In all the panels, * represents $p < 0.05$, ** represents $p < 0.01$, *** represents $p < 0.001$, and **** represents $p < 0.0001$).

Effect on apoptosis and cell proliferation

At the culmination of the 21-day period, tumor sections were obtained and subjected to the TUNEL assay to evaluate the initiation of apoptosis. The results revealed the highest level of apoptosis within the spH NPs-treated group, followed by PTX, RSQ, and PTX+RSQ groups (as depicted in **Figure 14A**). Uncontrolled proliferation stands as a hallmark of cancer. Ki67 serves as a widely accepted marker for proliferation and is frequently employed in standard pathological assessments of cancer due to its clinical relevance to metastasis and cancer stage. In the context of this research, we examined Ki67 expression in tumors collected after 21 days of treatment through immune-histofluorescence analysis. Remarkably, the expression of Ki67 in animals treated with spH NPs was notably lower when contrasted with animals treated with PTX+RSQ and the individual drug treatments (as shown in **Figure 14B**).

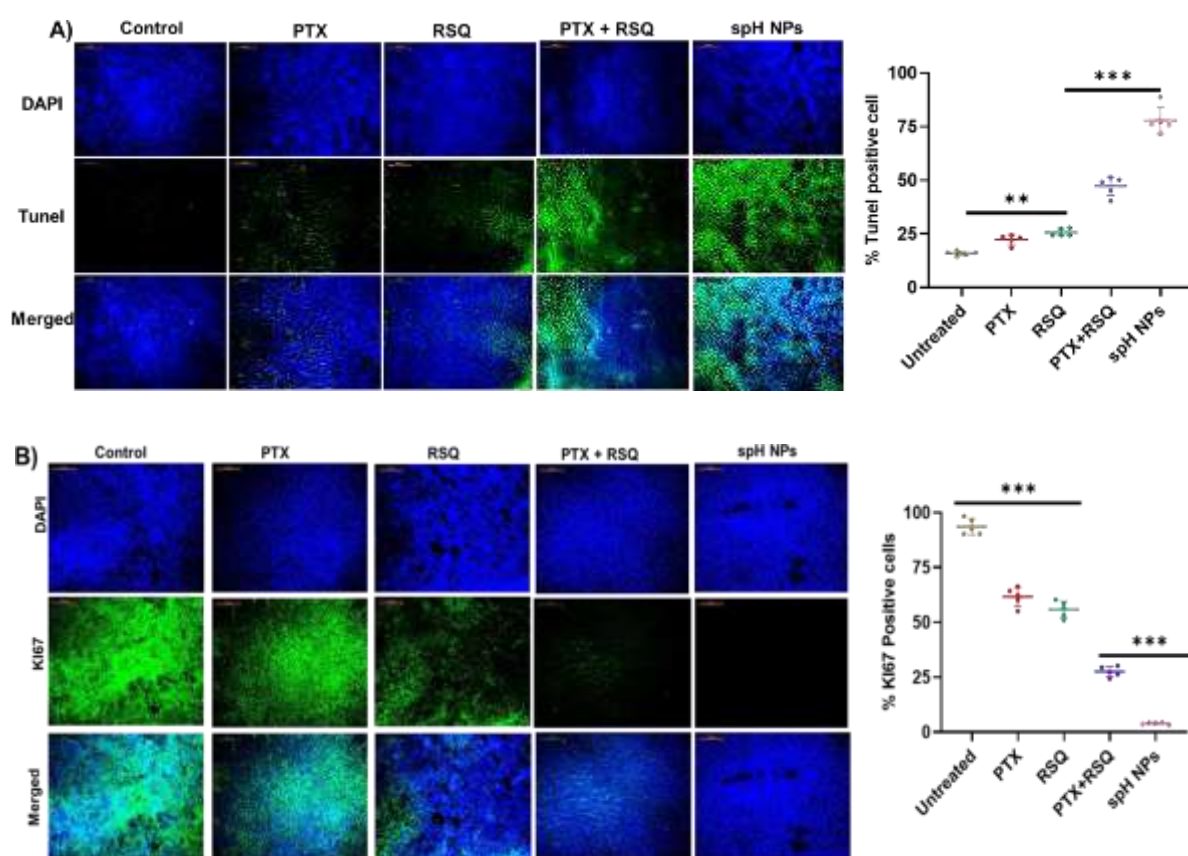


Figure 14. Effect of PTX+ RSQ loaded NPs treatment on tumor **A** Evaluation of apoptosis in tumor tissues by TUNEL assay. Quantification of fluorescence from TUNEL assay. **B** Evaluation of cell proliferation in tumor tissues by Ki67 immunohistofluorescence assay. Quantification of fluorescence from Ki-67 assay. (In all the panels, * represents $p < 0.05$, ** represents $p < 0.01$, *** represents $p < 0.001$, **** represents $p < 0.0001$, and ns represents no significant difference).

Effect on ROS

We noted a synergistic promotion of cancer cell apoptosis through the generation of reactive oxygen species (ROS) upon combining PTX with RSQ. Thus, our objective was to investigate the production of ROS within tumor tissue in response to NP formulations in an *in-vivo* setting. On the 21st day, the levels of ROS were quantified by measuring DCFH-DA fluorescence using the IVIS-Lumina in-vivo imaging system from PerkinElmer, Inc., USA (as depicted in Figure 15).

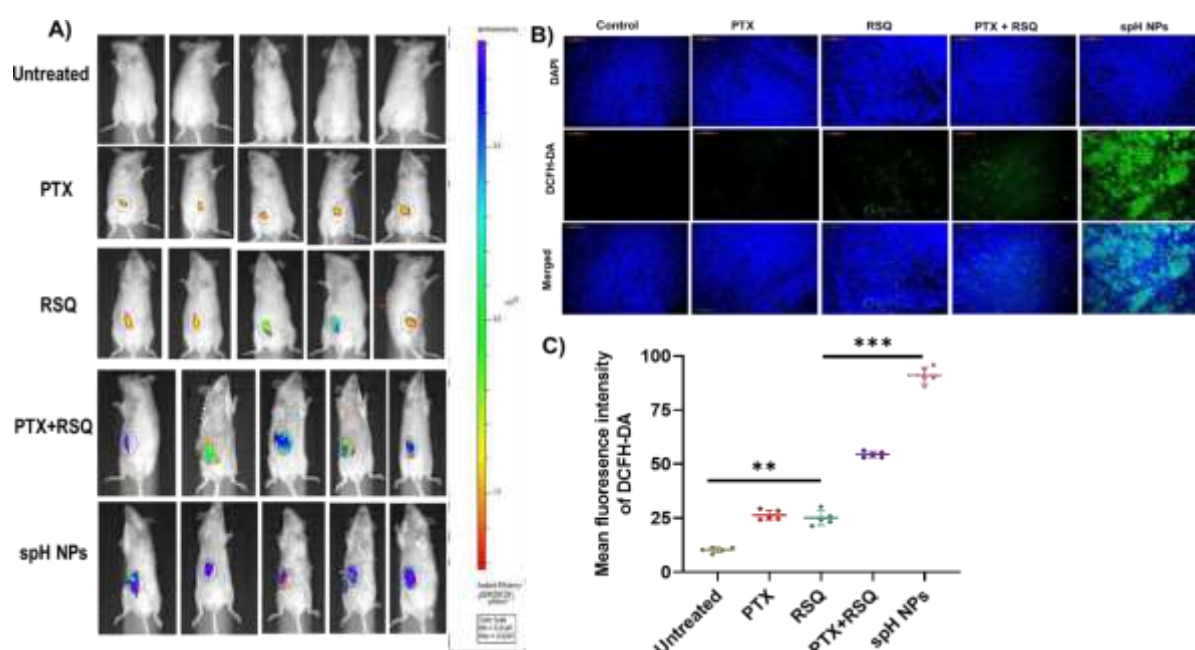


Figure 15. In-vivo ROS analysis. **A** DCFH-DA fluorescent images of the whole body of the mice with different treatments. **B** DAPI (blue) and DCFH-DA (green) fluorescence images of the sectioned tumor tissues. **C** fluorescent intensity analysis. (** represents $p < 0.01$, **** represents $p < 0.0001$).

Effect on metastasis

From a clinical perspective, more than 90% of breast cancer-related fatalities can be traced back to metastasis, with the lungs standing out as the primary destination for breast cancer metastatic spread. Given this context, our focus was directed towards examining the potential of the developed formulations to influence the metastatic behavior of breast tumors. Subsequent to the removal of tumors on the 21st day, a 9-day monitoring period was initiated to observe metastatic events. The evaluation of metastasis was carried out by measuring luciferin-induced bioluminescence emanating from the 4T1-Luc cells.

The control group exhibited prominent lung metastasis, and substantial bioluminescent signals were similarly detected in the PTX, RSQ, and PTX+RSQ groups. In stark contrast, the spH

NPs group exhibited no noticeable signal (as depicted in **Figure 16A**). More precisely, both the control and drug-treated groups (PTX, RSQ, PTX+RSQ) displayed significantly elevated luminescence compared to the groups treated with NPs. Among them, the control group had the highest cumulative lung bioluminescence, followed by the PTX, RSQ, and PTX+RSQ groups. Moreover, the spH NPs demonstrated the lowest overall lung weight (**Figure 16D**).

BrdU, which serves as an analogue of the nucleoside thymidine, is employed in the BrdU assay to identify actively proliferating cells. Consequently, it stands as a crucial marker in discerning

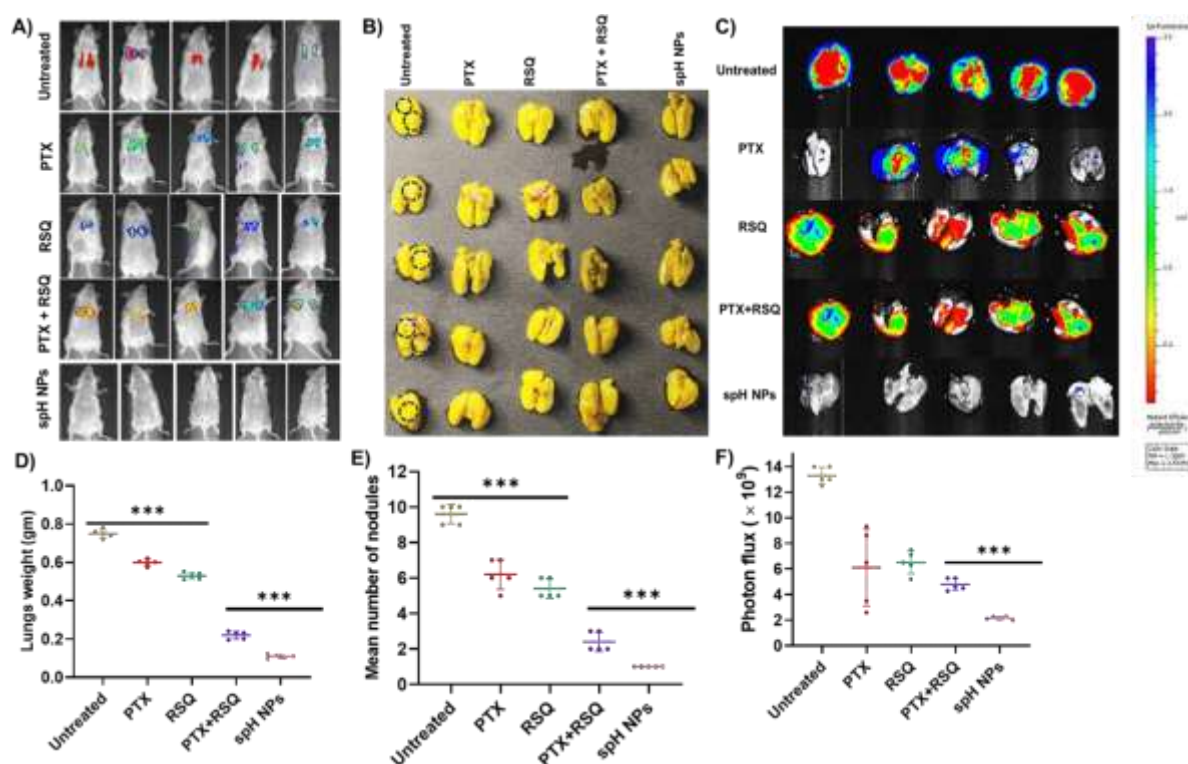


Figure 16. Analysis of in-vivo tumor metastasis. **A** Tumor metastasis was assessed by whole animal bioluminescence imaging of 4T1-Luc tumors. **B** Isolated lungs image of 4T1 Luc tumor. **C** Bioluminescence imaging of lung metastatic 4T1-Luc tumors. **D** Analysis of lung weight, **E** Number of metastatic nodules in lungs, **F** Analysis of bioluminescence of 4T1-Luc tumor metastasis to lungs. (In all the panels, * represents $p < 0.05$, ** represents $p < 0.01$, *** represents $p < 0.001$, and **** represents $p < 0.0001$).

cellular proliferation. The lung sections stained with BrdU were subjected to microscopic examination, revealing that the count of proliferating endothelial cells in lungs affected by metastasis was significantly higher in both the untreated group and the spH NPs group, as opposed to the other treatment groups (as depicted in **Figure 17**). This observation might be attributed to the potential entrapment of cancer cells within vessels, subsequently leading to

the formation of metastatic foci within the lungs. Furthermore, the spH NPs treated group exhibited a reduction in collagen levels when compared to the untreated group.

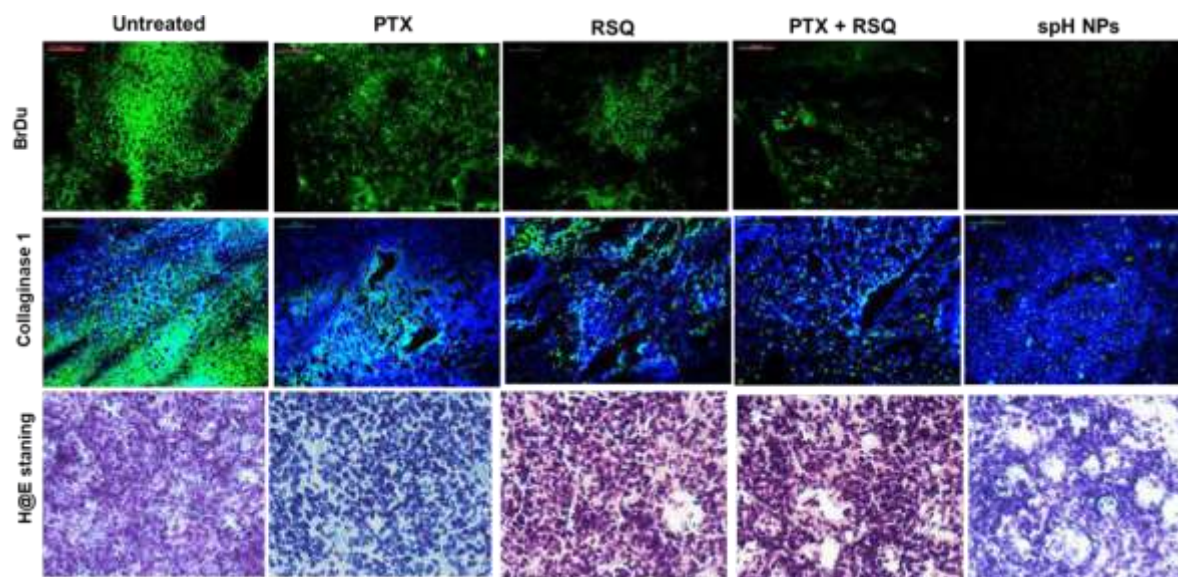


Figure 17. Suppression of lung metastasis. Proliferation of the metastatic cells in lung tissue detected by injecting BrdU into tail vein, followed by lung resection 2 h and stained with anti-BrdU antibody. The section was stained with collagen1A1 antibody to see the collagen level in lung. H&E staining of lung section showed more proliferation of cells compared to treatment groups.

Discussion

TAMs are the most abundant immune cells present in the TME in almost all types of solid tumors, and they play a vital role in regulating tumor growth.^{26,27} TAM-targeted therapies are primarily designed for TAM depletion; however, it was found that TAM depletion did not show required anti-cancer activity.²⁸ An alternative therapeutic approach is re-educating TAMs, which can actively promote anti-tumor immune responses and could be more efficacious.²⁹⁻³¹ Several approaches have been proposed for re-educating the TAMs, among which the use of TLR-agonists is a highly effective one.³² Different TLR-agonists have been evaluated for cancer therapy, exhibiting mixed responses.³² Different NP-based platforms have also been tested for tumor-targeted delivery of TLR-agonists. For example, Smith *et al.* demonstrated improved efficacy of a TLR7/8-agonist delivered using a PEG-PLANP.³³ Treatment with this NP was found to enhance the activity of anti-PD-L1 immunotherapy in a mouse colon carcinoma model. Schau *et al.* developed an NP delivery system of Riboxol, a TLR3 agonist, using a tumor-targeted, antibody fragment-conjugated NP, which produced a type I-interferon response in bladder cancer cells.³⁴ The delivery of a TLR-3 agonist poly(I:C) using a calcium phosphate NP resulted in improved immune stimulation.³⁵ These studies established the superior efficacy of NP-mediated immunotherapy with TLR-agonists. Considerable research

has also been done on NP-based combined chemo-immunotherapy. Roy *et al.* have developed an NP formulation to deliver PTX and a TLR-4 agonist (P/SP-LPS). They have reported two different types of formulations: in one, both the chemotherapeutic drug and the immune-modulator were co-encapsulated in a PLGA NP,^{36,37} in the other, both PTX and SP-LPS were conjugated to form a micellar NP formulation.³⁸ Both the nano-formulations exhibited significantly better therapeutic efficacy than either of the components alone in *in-vivo* studies against a murine melanoma model. It also converted the immunosuppressive tumor microenvironment into an immune stimulatory state compared to only minor stimulation with the TLR-4 agonist alone, highlighting the potential advantage of combined chemo-immunotherapy.^{37,38} Hu *et al.* have demonstrated that NP-mediated co-delivery of PTX and IL-12 resulted in increased T cell and NK cell activation, reduction in T_{reg} cells, induction of M1-macrophages, and ultimately, increased survival of tumor-bearing mice.³⁹ Pauli *et al.* developed a liposomal formulation of RSQ, which, combined with oxaliplatin treatment, exhibited significantly increased infiltration of CD8+ T cells in the tumor.⁴⁰

In the current study, different TLR-agonists were initially screened for macrophage stimulation. Among them, TLR7/8 agonist RSQ was found to be the most potent one (**Figure 1B**). Multiple studies have reported high efficacy of RSQ as cancer immunotherapy, signifying it can augment immunity and potentiate anti-cancer therapeutic efficacy.¹⁷⁻¹⁹ However, no report could be found evaluating the efficacy of the combination of PTX and RSQ. In this study, a significant improvement in the combined chemo-immunotherapeutic efficacy of the PTX+RSQ combination was observed (**Figure 1D**). A pH-sensitive nano-formulation was conceived to evaluate their efficacy when co-encapsulated in an NP formulation. Designing nano-formulations for multi-drug delivery (in which different drug targets different cells) is significantly more challenging than single drug-loaded NPs. Nano-carriers, like liposomes, polymeric NPs, micelles, and drug-conjugates, can be taken up by cells,⁴¹ and the drug/s encapsulated in that nano-carrier would be effective against that cell only. Hence, a multi-drug-loaded nano-carrier targeting different types of cells should release the drugs efficiently upon reaching the TME so that the drug combination can act on their specific target cells. In this study, a pH-responsive polymer for TME targeted drug release was synthesized. The extracellular pH in the TME is more acidic (pH 6.5 to 6.9) than the normal physiological pH (pH 7.2 to 7.5) due to the increased glycolysis and accumulation of lactic acid in the TME.⁴² This lower pH in the TME was exploited for the NP's TME-specific release of PTX and RSQ. Due to the imidazole ring that contains a lone pair of electrons on the unsaturated

nitrogen atom, histidine can undergo pH-dependent protonation-deprotonation and polarity. Histidine remains in the non-protonated form at physiological pH, favoring interactions with other hydrophobic groups. At pH below its pKa, the imidazole ring becomes protonated and undergoes solubility transition, which can function as an efficient pH-sensitive moiety.⁴³ It has also been observed that histidine is responsible for the endosomal escape of the NPs because of its high pH buffering ability which is commonly known as the proton sponge effect.⁴⁴

In this study, pH-sensitive polymers were synthesized by conjugating poly-histidine moiety with a five armed-PLGA (s-PLGA-pH) (**Scheme 1**) and a linear PLGA (l-PLGA-pH) and compared their efficacy for the co-delivery of PTX and RSQ. Increased PTX and RSQ loading was observed in the s-PLGA-pH NPs (**Table 1**). Earlier studies have demonstrated the impact of the polymer shape on drug loading and drug release.⁴⁵ It has been proven that multi-armed polymers have more drug loading than linear polymers.⁴⁶ In the drug release study, both l-PLGA-pH and s-PLGA-pH NPs exhibited increased drug release at lower pH than neutral pH; however, with the s-PLGA-pH NPs, the drug release ratio between PTX and RSQ was almost 1:1, which was not observed in l-PLGA-pH NPs (**Figure 6**). Maintaining the specific dose ratio could be beneficial for synergistic activity. The hypothesis was that in the case of the l-PLGA-pH NPs, only one end of the polymer was ionizing. However, the body of the polymer remained stable, which could lead to differential drug release. In the case of s-PLGA-pH NPs, due to histidine modification at the end of each arm of its multi-arm structure, ionization would lead to the same charge repulsion among all the arms, leading to complete opening of the NPs, releasing the encapsulated drug entirely. This hypothesis was supported by the NP size variation at different pHs (**Figure 5** and **Table 2**).

The pH-sensitive delivery of the drug combination can influence its bioactivity. Against only cancer cells, similar cytotoxic potency was observed with the drug combination, both free and NP encapsulated (**Figure 7A**). However, when tested against a complex spheroid model comprised of cancer and macrophage cells that mimics actual tumors, the pH-sensitive s-PLGA-pH NPs exhibited significantly increased efficacy in cancer cell killing (**Figure 7D**). This could be due to improved spheroid core delivery of the encapsulated drugs by the s-PLGA-pH NPs. Thereafter live dead staining using transwell system containing 3D tumor spheroids and 2D macrophage, we have observed almost no cell death with macrophages and increased tumor specific cell death with increased PI in 3D tumor spheroids. It is also evident that, the PI stain, which stains the nucleus of dead cells is high in case of NPs but not in free drug combination (PTX +RSQ), which might be because of the high permeability of the drugs when

given in NPs, because of their pH-sensitive drug release, at the spheroid acidic pH, NP is getting destabilized and permeating more into the spheroid which in turn is resulting in tumor cell death, but when coming to the free drugs, PI staining is less which might be because of low permeability of the free drugs. (**Figure 8**). To analyze the spheroid core penetration by the NP-encapsulated drugs, microscopic evaluation of fluorescent-tagged (DiI-loaded) l-PLGA-pH and s-PLGA-pH NPs were done in the cancer spheroid model. A significant increased cancer spheroid core penetration was observed with the s-PLGA-pH NPs (**Figure 9**). Treatment with s-PLGA-pH NPs also exhibited reversal of the M2-phenotype of cancer-associated macrophages to an M1-phenotype, indicating robust immune activation (**Figure 10**).

After successful determination of pH sensitivity and in-vitro anti-tumor efficacy of the NPs, we further moved into in-vivo analysis, Where initial toxicity study has proven that there are no signs of toxicity and necrosis in all the groups no inflammation and fibrosis, with histology of all the organs i.e., lung, liver, kidney, spleen and heart as intact similar to control proving that the doses used are non-toxic within this period. Thereafter PK profiles were also found to be improved with both PTX and RSQ when given in spH NPs form when compared to free drug alone and combination as well (**Figure 11**). Additionally, increased tumor accumulation of sp and spH NPs when compared to other organs because of extended plasma half-life of NPs, as we have observed in PK study. But increased DiI fluorescence with spH NPs in tumor tissue when compared to sp NPs might be because of our previous observations in in-vitro analysis, i.e., enhanced delivery of payload of spH in 3D tumor model, suggesting that pH sensitive nature helped in release at tumor extra cellular pH, leading to enhanced tumor accumulation which could lead to improved efficacy of drugs (**Figure 12**). Further the in-vivo analysis has shown that improved efficacy with decreased tumor volume in spH NPs when compared to other treatment groups along with increased apoptosis which might be due to increased circulation time and tumor-specific accumulation of nanoparticles (**Figure 13**). It is well known that uncontrolled proliferation is a characteristic feature of cancers. Ki67 is used as a proliferation marker in routine pathological investigations of cancer as it is strongly associated with cell proliferation and clinically correlates with metastasis and the clinical stage of tumors. Hence, Ki67 analysis helps in determining the clinical outcome of therapy, with basal level ki67 expression with spH NPs when compared to free drug alone and combination by substantiating the results of tumor volume analysis (**Figure 14**). Interestingly, we have also found Significantly higher induction of ROS observed with spH NPs supporting the induction of apoptosis with TUNEL assay (**Figure 15**). Clinically, about > 90% of breast cancer-related

deaths are due to metastasis. Breast cancer most commonly metastasizes to the lungs and bones. Total animal bioluminescence imaging showed significant lung metastasis in the control group. In the PTX, RSQ, and PTX + RSQ groups, some amount of metastasis was observed, but no signal was observed in the spH NPs. The same trend was observed in the total weight of lungs and the number of metastatic nodules. Lung weight and total bioluminescence in spH NPs were lower than in other groups, and H&E staining of lung sections showed the extent of tumor metastasis to the lungs; with spH NPs, metastasis was significantly less, proving the reduced lung metastasis compared to other treatments (**Figure 16,17**) indicating its effectiveness against TME-intrinsic resistance.

The current study demonstrated that the PTX and RSQ combination could effectively target macrophages by converting immunoinhibitory macrophages (M2) to immunostimulatory macrophages (M1) in both in-vitro and in-vivo delivery. Thus, this drug combination using soluplus-decorated pH-sensitive NPs could increase tumor accumulation, resulting in improved anti-tumor efficacy. This formulation can be extended to other solid tumors for which PTX efficacy is limited due to its low circulation time and development of resistance and in combination with other immunotherapeutic strategies.

IMPACT OF THE RESEARCH

Anticancer therapy has evolved significantly in the last few decades. In the early years, cancer was considered to be a disease of neoplastic cells only. Escalating global cancer prevalence underscores the urgent need for innovative solutions. Due to this, the highly proliferating cancer cells are the lone target against which almost all of the anticancer drugs were developed. However, the clinical efficacy of these cytotoxic drugs was marginal. Owing to many advanced studies, it has been established that tumors are a complex network of neoplastic and non-neoplastic cells intertwining in a strong symbiotic relationship, which provides the condition permissive for the growth and progression of malignant cells. It is becoming clear that the traditional one-dimensional approach to cancer treatment may not be sufficient. A multi-dimensional treatment modality needs to be developed for a more successful treatment.

As a strategy, combined chemo-immunotherapy has gained significant interest in the last few years. However, developing a specifically designed delivery system for such multi-dimensional therapy is still in its infancy. The delivery of a multi-dimensional drug combination is more complicated than the delivery of a single drug. As different drugs target different types of cells, their bioavailability in the tumor microenvironment is critical. A triggered release approach

will solve this problem. Different types of triggered release strategies have been evaluated previously. Among them, pH-sensitive NPs are the most advanced for clinical application and can be used for precise and localized therapy in a clinical setting.

In our study, Initial screening identified the most effective TLR-agonist, RSQ, combined with PTX. Comparative analysis of pH-sensitive nano-delivery systems highlighted a multi-armed, star-shaped polymer's superiority, enhancing pH-dependent size variation, drug release, and spheroid penetration. The multi-arm polymer exhibited enhanced combined chemo-immunotherapeutic activity. In vivo safety validation and improved PTX and RSQ plasma circulation were observed with stimuli-responsive NPs. The combined treatment demonstrated superior anti-cancer effects, inducing apoptosis, ROS generation, and metastasis inhibition. The research suggests potent chemo-immunotherapeutic activity with clinical potential.

The improved efficacy analysis of the drug combination in macrophage - tumor cell co-culture system-2D and 3D as well as in-vivo with a significant increase in cell death. Along with advanced pre-clinical, as well as clinical studies, have indicated that combination of chemotherapy and immunotherapy can be a highly potential strategy for the treatment of cancer. However, clinical implementation is lagging due to the absence of a suitable delivery system for such a multi-dimensional treatment modality. We believe our research would be able to fill that void which can radically change cancer treatment approach.

This approach could reshape cancer treatment by addressing current challenges and benefiting patients. The pH-sensitive nanoparticle delivery system's precision minimizes side effects, while the dual therapy strategy synergizes chemotherapy and immunotherapy, potentially enhancing survival rates and patients' quality of life. This research pioneers medical nanotechnology by developing pH-sensitive nanoparticles. It underscores the interdisciplinary collaboration between chemistry, engineering, and biology, contributing to our understanding of nanomedicine's potential. The research signifies a pivotal advancement in cancer treatment, offering the potential to improve outcomes, reduce side effects, and expand our understanding of medical nanotechnology. Its far-reaching impact on patient well-being and broader scientific knowledge underscores its significance in advancing global health and well-being.

References

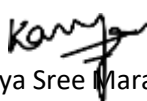
1. Azamjah N, Soltan-Zadeh Y, Zayeri F. Global Trend of Breast Cancer Mortality Rate: A 25-Year Study. *Asian Pac J Cancer Prev*. 2019;20(7):2015-2020. <https://doi.org/10.31557/APJCP.2019.20.7.2015>.
2. Lima SM, Kehm RD, Terry MB. Global breast cancer incidence and mortality trends by region, age-groups, and fertility patterns. *EClinicalMedicine*. 2021;38:100985. <https://doi.org/10.1016/j.eclinm.2021.100985>.
3. Hudis CA, Gianni L. Triple-negative breast cancer: an unmet medical need. *Oncologist*. 2011;16 Suppl 1:1-11. <https://doi.org/10.1634/theoncologist.2011-S1-01>.
4. Williams CB, Yeh ES, Soloff AC. Tumor-associated macrophages: unwitting accomplices in breast cancer malignancy. *NPJ Breast Cancer*. 2016;2. <https://doi.org/10.1038/npjbcancer.2015.25>.
5. Waks AG, Winer EP. Breast Cancer Treatment: A Review. *JAMA*. 2019;321(3):288-300. <https://doi.org/10.1001/jama.2018.19323>.
6. Roy A, Li SD. Modifying the tumor microenvironment using nanoparticle therapeutics. *Wiley Interdiscip Rev Nanomed Nanobiotechnol*. 2016;8(6):891-908. <https://doi.org/10.1002/wnan.1406>.
7. Seebacher NA, Krchniakova M, Stacy AE, Skoda J, Jansson PJ. Tumour Microenvironment Stress Promotes the Development of Drug Resistance. *Antioxidants (Basel)*. 2021;10(11). <https://doi.org/10.3390/antiox10111801>.
8. Wu P, Gao W, Su M, et al. Adaptive Mechanisms of Tumor Therapy Resistance Driven by Tumor Microenvironment. *Front Cell Dev Biol*. 2021;9:641469. <https://doi.org/10.3389/fcell.2021.641469>.
9. Kaemmerer E, Loessner D, Avery VM. Addressing the tumour microenvironment in early drug discovery: a strategy to overcome drug resistance and identify novel targets for cancer therapy. *Drug Discov Today*. 2021;26(3):663-676. <https://doi.org/10.1016/j.drudis.2020.11.030>.
10. Gonzalez H, Hagerling C, Werb Z. Roles of the immune system in cancer: from tumor initiation to metastatic progression. *Genes Dev*. 2018;32(19-20):1267-1284. <https://doi.org/10.1101/gad.314617.118>.
11. Gun SY, Lee SWL, Sieow JL, Wong SC. Targeting immune cells for cancer therapy. *Redox Biol*. 2019;25:101174. <https://doi.org/10.1016/j.redox.2019.101174>.
12. Petty AJ, Yang Y. Tumor-associated macrophages: implications in cancer immunotherapy. *Immunotherapy*. 2017;9(3):289-302. <https://doi.org/10.2217/imt-2016-0135>.
13. Chen Y, Song Y, Du W, Gong L, Chang H, Zou Z. Tumor-associated macrophages: an accomplice in solid tumor progression. *J Biomed Sci*. 2019;26(1):78. <https://doi.org/10.1186/s12929-019-0568-z>.
14. Zheng X, Turkowski K, Mora J, et al. Redirecting tumor-associated macrophages to become tumoricidal effectors as a novel strategy for cancer therapy. *Oncotarget*. 2017;8(29):48436-48452. <https://doi.org/10.18632/oncotarget.17061>.
15. Yin T, He S, Wang Y. Toll-like receptor 7/8 agonist, R848, exhibits antitumoral effects in a breast cancer model. *Mol Med Rep*. 2015;12(3):3515-3520. <https://doi.org/10.3892/mmr.2015.3885>.
16. Wang S, Yang Y, Ma P, et al. Landscape and perspectives of macrophage -targeted cancer therapy in clinical trials. *Mol Ther Oncolytics*. 2022;24:799-813. <https://doi.org/10.1016/j.omto.2022.02.019>.
17. Zhang H, Tang WL, Kheirrolomoom A, et al. Development of thermosensitive resiquimod-loaded liposomes for enhanced cancer immunotherapy. *J Control Release*. 2021;330:1080-1094. <https://doi.org/10.1016/j.jconrel.2020.11.013>.

18. Figueiredo P, Lepland A, Scodeller P, et al. Peptide-guided resiquimod-loaded lignin nanoparticles convert tumor-associated macrophages from M2 to M1 phenotype for enhanced chemotherapy. *Acta Biomater.* 2021;133:231-243. <https://doi.org/10.1016/j.actbio.2020.09.038>.
19. Chen PM, Pan WY, Wu CY, et al. Modulation of tumor microenvironment using a TLR-7/8 agonist-loaded nanoparticle system that exerts low-temperature hyperthermia and immunotherapy for in situ cancer vaccination. *Biomaterials.* 2020;230:119629. <https://doi.org/10.1016/j.biomaterials.2019.119629>.
20. Long HJ. Paclitaxel (Taxol): a novel anti-cancer chemotherapeutic drug. *Mayo Clin Proc.* 1994;69(4):341-345. [https://doi.org/10.1016/s0025-6196\(12\)62219-8](https://doi.org/10.1016/s0025-6196(12)62219-8).
21. Zhu L, Chen L. Progress in research on paclitaxel and tumor immunotherapy. *Cell Mol Biol Lett.* 2019;24:40. <https://doi.org/10.1186/s11658-019-0164-y>.
22. van der Meel R, Sulheim E, Shi Y, Kiessling F, Mulder WJM, Lammers T. Smart cancer nanomedicine. *Nat Nanotechnol.* 2019;14(11):1007-1017. <https://doi.org/10.1038/s41565-019-0567-y>.
23. Hong W, Chen D, Jia L, et al. Thermo- and pH-responsive copolymers based on PLGA-PEG-PLGA and poly(L-histidine): synthesis and in vitro characterization of copolymer micelles. *Acta Biomater.* 2014;10(3):1259-1271. <https://doi.org/10.1016/j.actbio.2013.12.033>.
24. Dao TPT, Nguyen TH, To VV, Ho TH, Nguyen TA, Dang MC. A new formulation of curcumin using poly (lactic-co-glycolic acid)-polyethylene glycol diblock copolymer as carrier material. *Advances in Natural Sciences-Nanoscience and Nanotechnology.* 2014;5(3). <https://doi.org/Arttn> 035013
- 10.1088/2043-6262/5/3/035013.
25. Barrera-Rodriguez R, Fuentes JM. Multi-drug resistance characterization in multi-cellular tumour spheroids from two human lung cancer cell lines. *Cancer Cell Int.* 2015;15:47. <https://doi.org/10.1186/s12935-015-0200-6>.
26. Steidl C, Lee T, Shah SP, et al. Tumor-associated macrophages and survival in classic Hodgkin's lymphoma. *N Engl J Med.* 2010;362(10):875-885. <https://doi.org/10.1056/NEJMoa0905680>.
27. Joyce JA, Pollard JW. Microenvironmental regulation of metastasis. *Nat Rev Cancer.* 2009;9(4):239-252. <https://doi.org/10.1038/nrc2618>.
28. Franklin RA, Li MO. Ontogeny of Tumor-associated Macrophages and Its Implication in Cancer Regulation. *Trends Cancer.* 2016;2(1):20-34. <https://doi.org/10.1016/j.trecan.2015.11.004>.
29. Ruffell B, Coussens LM. Macrophages and therapeutic resistance in cancer. *Cancer Cell.* 2015;27(4):462-472. <https://doi.org/10.1016/j.ccell.2015.02.015>.
30. Mantovani A, Allavena P. The interaction of anti-cancer therapies with tumor-associated macrophages. *J Exp Med.* 2015;212(4):435-445. <https://doi.org/10.1084/jem.20150295>.
31. Movahedi K, Laoui D, Gysemans C, et al. Different tumor microenvironments contain functionally distinct subsets of macrophages derived from Ly6C(high) monocytes. *Cancer Res.* 2010;70(14):5728-5739. <https://doi.org/10.1158/0008-5472.CAN-09-4672>.
32. Adams S. Toll-like receptor agonists in cancer therapy. *Immunotherapy.* 2009;1(6):949-964. <https://doi.org/10.2217/imt.09.70>.
33. Smith AAA, Gale EC, Roth GA, et al. Nanoparticles Presenting Potent TLR7/8 Agonists Enhance Anti-PD-L1 Immunotherapy in Cancer Treatment. *Biomacromolecules.* 2020;21(9):3704-3712. <https://doi.org/10.1021/acs.biomac.0c00812>.
34. Schau I, Michen S, Hagstotz A, et al. Targeted delivery of TLR3 agonist to tumor cells with single chain antibody fragment-conjugated nanoparticles induces type I-interferon

- response and apoptosis. *Sci Rep*. 2019;9(1):3299. <https://doi.org/10.1038/s41598-019-40032-8>.
35. Sokolova V, Shi Z, Huang S, et al. Delivery of the TLR ligand poly(I:C) to liver cells in vitro and in vivo by calcium phosphate nanoparticles leads to a pronounced immunostimulation. *Acta Biomater*. 2017;64:401-410. <https://doi.org/10.1016/j.actbio.2017.09.037>.
 36. Roy A, Singh MS, Upadhyay P, Bhaskar S. Combined chemo-immunotherapy as a prospective strategy to combat cancer: a nanoparticle based approach. *Mol Pharm*. 2010;7(5):1778-1788. <https://doi.org/10.1021/mp100153r>.
 37. Roy A, Singh MS, Upadhyay P, Bhaskar S. Nanoparticle mediated co-delivery of paclitaxel and a TLR-4 agonist results in tumor regression and enhanced immune response in the tumor microenvironment of a mouse model. *Int J Pharm*. 2013;445(1-2):171-180. <https://doi.org/10.1016/j.ijpharm.2013.01.045>.
 38. Roy A, Chandra S, Mamilapally S, Upadhyay P, Bhaskar S. Anticancer and immunostimulatory activity by conjugate of paclitaxel and non-toxic derivative of LPS for combined chemo-immunotherapy. *Pharm Res*. 2012;29(8):2294-2309. <https://doi.org/10.1007/s11095-012-0756-y>.
 39. Hu Q, Shang L, Wang M, et al. Co-Delivery of Paclitaxel and Interleukin-12 Regulating Tumor Microenvironment for Cancer Immunochemotherapy. *Adv Healthc Mater*. 2020;9(10):e1901858. <https://doi.org/10.1002/adhm.201901858>.
 40. Pauli G, Chao PH, Qin Z, Bottger R, Lee SE, Li SD. Liposomal Resiquimod for Enhanced Immunotherapy of Peritoneal Metastases of Colorectal Cancer. *Pharmaceutics*. 2021;13(10). <https://doi.org/10.3390/pharmaceutics13101696>.
 41. Donahue ND, Acar H, Wilhelm S. Concepts of nanoparticle cellular uptake, intracellular trafficking, and kinetics in nanomedicine. *Adv Drug Deliv Rev*. 2019;143:68-96. <https://doi.org/10.1016/j.addr.2019.04.008>.
 42. Feng L, Dong Z, Tao D, Zhang Y, Liu Z. The acidic tumor microenvironment: a target for smart cancer nano-theranostics. *National Science Review*. 2017;5(2):269-286. <https://doi.org/10.1093/nsr/nwx062> %J National Science Review.
 43. Li S, Hong M. Protonation, tautomerization, and rotameric structure of histidine: a comprehensive study by magic-angle-spinning solid-state NMR. *J Am Chem Soc*. 2011;133(5):1534-1544. <https://doi.org/10.1021/ja108943n>.
 44. Swetha KL, Maravajjala K, Sharma S, Chowdhury R, Roy A. Development of a tumor extracellular pH-responsive nano-carrier by terminal histidine conjugation in a star shaped poly(lactic-co-glycolic acid). *European Polymer Journal*. 2021;147. <https://doi.org/ARTN110337,10.1016/j.eurpolymj.2021.110337>.
 45. Chen Y, Yang Z, Liu C, et al. Synthesis, characterization, and evaluation of paclitaxel loaded in six-arm star-shaped poly(lactic-co-glycolic acid). *Int J Nanomedicine*. 2013;8:4315-4326. <https://doi.org/10.2147/IJN.S51629>.
 46. Tao W, Zeng X, Liu T, et al. Docetaxel-loaded nanoparticles based on star-shaped mannitol-core PLGA-TPGS diblock copolymer for breast cancer therapy. *Acta Biomater*. 2013;9(11):8910-8920. <https://doi.org/10.1016/j.actbio.2013.06.034>.

Date: 30/08/2023

Place: Pilani


Kavya Sree Maravajjala
(Ph.D. Research Scholar)